Measurement of TeV gamma-ray spectra with the Cherenkov imaging technique

G. Mohanty [a,f], S. Biller [b], D.A. Carter-Lewis [a], D.J. Fegan [d], A.M. Hillas [b], R.C. Lamb [c], T.C. Weekes [e], M. West [b], J. Zweerink [a]

[a] *Department of Physics and Astronomy, Iowa State University, Ames, IA 50011-3160, USA*
[b] *Department of Physics and Astronomy, University of Leeds, Leeds LS2 9JT, UK*
[c] *Space Radiation Laboratory, Caltech, Pasadena, CA, USA*
[d] *Physics Department, University College Dublin, Dublin, Ireland*
[e] *Harvard–Smithsonian CfA, Fred Lawrence Whipple Observatory, P.O. Box 97, Amado, Arizona 85645-0097, USA*
[f] *Presently at LPNHE Ecole Polytechnique, 91128 Palaiseau Cedex, France*

Abstract

In this paper, we seek to establish reliable methods for extracting energy spectra for TeV gamma-ray sources observed using the atmospheric Cherenkov Imaging Technique. Careful attention has been paid to the calculation of the telescope gain, and we obtain good agreement between direct measurements, with a statistical error of about 10%, and an absolute calibration from the background cosmic-ray trigger rate that has an overall error of 18%. Two independent analyses that are based on different Monte Carlo shower simulations, employ different selection criteria in order to retain a large fraction of gamma-ray events, and use different approaches to spectral estimation are presented here. The first is a fairly traditional method that builds on established image selection techniques and calculates the detector collection area and an energy estimation function. The error in measuring the enrgy of a single event is estimated at 36%, and we try to compensate for this poor energy resolution. The second analysis uses more elegant gamma-ray selection criteria and implicitly incorporates the properties of the detector into the simulations that are then compared with the data in order to obtain source spectra. The two simulations are compared to each other and to the data, with the aim of establishing that each method is robust and insensitive to simulation details. Finally, we consider the main sources of systematic errors, the largest of which is in the telescope gain calibration, arising from an incomplete knowledge of the relevant factors, and is estimated to be 16%. The effect of possible errors in the simulations is also considered.

Both methods have been applied to a part of the Whipple observatory database on the Crab Nebula for the 1988/89 observing season, while the first method has also been applied to data taken in 1995/96. The statistical error in the flux constant is about 8% and that in the spectral index is about 5%, while the corresponding systematic errors are estimated to be 18% and 2%, respectively. The results presented here show good agreement between the two methods as well as between the two seasons. However, a comprehensive consideration of the implications of the derived spectra and a comparison to other work is addressed in another paper. © 1998 Elsevier Science B.V.

Keywords: Gamma rays; General stars; Individual (Crab Nebula)

1. Introduction

The Cherenkov Imaging Technique has been pivotal in establishing the existence of discrete cosmic sources of TeV gamma-rays (see, e.g., Cronin et al., 1993). With this technique, it is also possible to map out temporal variations of these sources (Kerrick et al., 1995), pin down source locations in the sky (Akerlof et al., 1991) and infer energy spectra (Macomb, 1989; Plyasheshnikov and Konopelko, 1989a; Plyasheshnikov and Konopelko, 1989b; Vacanti et al., 1991; Lewis et al., 1993; Mohanty et al., 1993; West, 1994; Mohanty, 1995). Images were characterized using combinations of first and second-order moments which measure the shape and orientation of the images. In particular, on the basis of a priori simulations, Hillas (1985) proposed using a single image parameter, *azwidth*, to differentiate gamma-ray showers from cosmic-ray background. Shower images with small values of *azwidth* were identified as likely to be gamma rays, and showers with larger values were more likely to be background. This was the basis for the detection of the Crab Nebula in Weekes et al. (1989).

The purpose of this paper is to describe in detail the methodologies developed by the Whipple collaboration for establishing the TeV gamma-ray spectra of cosmic point sources detected using the imaging atmospheric Cherenkov technique. Data taken on the Crab Nebula during the 1988/89 and 1995/96 observing seasons were used as a testbed for the methods to be described. A forthcoming publication (Hillas et al., 1997) discusses our results in greater detail and interprets them in the context of other work on the Crab Nebula.

There are several steps involved in obtaining spectra from Cherenkov imaging telescopes.

 (i) A method is needed to preferentially select gamma-ray images from the overwhelming cosmic-ray background. Generally, images meeting the selection criteria (e.g., a small *azwidth*) are retained in the data and events not meeting these criteria are rejected as background. For determination of a spectrum, the method must have *known efficiency* over a wide range of primary gamma-ray energies.

 (ii) The collection area of the telescope over a wide range of energies must be known. This area will depend upon the manner in which the telescope is "triggered" to record an image and on the efficiency of the gamma-ray selection method.

(iii) The energy of the primary gamma-ray must be estimated from the characteristics of the observed image. The energy estimation method may be chosen to optimize the energy resolution of the telescope.

(iv) Only the estimated primary energies are known, and if these are symmetrically distributed about the real energy for a rapidly falling spectrum, the fluxes in each estimated energy bin will be distorted by the finite energy resolution of the telescope. This has to be carefully taken into account in estimating the source energy spectrum which is expected to approximate a power law.

 (v) The telescope parameters (mirror reflectivity, pmt gains, etc.,) must be either directly measured, or estimated from the data. Even with perfect knowledge of the detector parameters, an uncertainty would be introduced by the incomplete knowledge of the atmospheric transmittivity for the Cherenkov light.

In this paper, we address these issues, approaching the task of extracting TeV gamma-ray energy spectra with two somewhat different methods of event selection, together with two independent sets of Monte Carlo shower simulation programs that have independent development histories. Method 1, developed mainly at Iowa State University, and Method 2, developed mainly at the University of Leeds. The first "extended supercuts" approach uses straightforward criteria to select gamma-ray-like images and the telescope collection area and resolution function are explicitly calculated. The spectrum is arrived at assuming a form close to a power law. In contrast, the second method ("cluster" or "ellipsoidal-window selection") uses a more elegant and efficient criterion for selecting gamma-ray-images and the spectrum is extracted by adjusting the input spectrum in Monte Carlo simulations to fit the observed distribution of the total light in the selected images. The collection area and resolution function need not be explicitly calculated. Both methods have been applied to the uniform and well-analyzed Whipple Observatory 1988/89 Crab Nebula database, and as an independent check, Method 1 has also been applied to the recent 1995/96 database which had a different camera configuration.

Crucial features of this paper are (i) the degree of detail which we have applied in the development of two

distinct methods for establishing the spectra of TeV sources, and (ii) careful cross-checking of the robustness of each method so that the results are relatively insensitive to small details. The general characteristics of an imaging Cherenkov telescope and methods of extracting spectra are detailed in Section 2. These methods are then applied to the Whipple Observatory Crab databases as described in Section 3.

2. Detection of TeV gamma-rays using the atmospheric imaging technique

This section describes the detection of the Cherenkov light in the extensive air showers produced by high-energy gamma rays in the atmosphere. A shower which generates sufficient light at the telescope will trigger it, causing it to record a digitized image consisting of the number of counts registered in each individual channel. This image is the basis for the identification of gamma-ray showers, and for the subsequent estimation of the energy of the primary gamma-ray. The relevant properties of the observed Cherenkov light are described in Section 2.1, while Section 2.2 gives the characteristics of the Whipple 10-meter telescope.

The properties of a Cherenkov telescope most relevant for the determination of spectra are telescope gain (Section 2.3), background rejection (Section 2.5), collection area (Section 2.6), and energy estimation (Section 2.7). As there is no calibrated source of cosmic TeV gamma rays, the determination of energy spectra necessarily depends on simulations. The simulations used are presented and compared in Section 2.4.

2.1. Cherenkov light characteristics

The lateral distribution of Cherenkov light from simulated vertical gamma-ray air showers at the Whipple Observatory altitude (2.3 km) is shown in Fig. 1 for gamma-ray energies of 0.4, 1.0, and 5.0 TeV. The lateral distribution has a characteristic shape with a central peak connecting to a relatively flat region leading out to a rim at about 120 meters. Beyond the rim, the light intensity falls rapidly. The photon density over the flat part of the curve is roughly proportional to the energy of the primary gamma-ray. The peak at the center is due to local, penetrating particles and becomes less pronounced with decreasing energy or increasing zenith angle. The rim at 120 meters arises from a compensating effect of smaller Cherenkov angles for light emitted at greater altitudes above the observer, in the range 7–15 km, and its position hardly varies with primary energy. Fluctuations of light intensity are relatively small near the rim and the total light recorded by a telescope there is a good measure of the primary energy. As the telescope is displaced toward the edge of the light pool from the shower, the centroid of the image moves outward in the field of view. For a telescope located at the rim, the centroid of the image on the focal plane is about 0.9° from the center of the field of view. For further discussion of shower characteristics, related in particular to distinguishing between gamma and hardronic showers, see Hillas (1996).

2.2. Data acquisition with the Whipple observatory's gamma-ray telescope

The Whipple Observatory 10-meter Gamma-ray Telescope is described in detail elsewhere (Cawley et al., 1990). At the time the 1988/89 Crab data were taken, the focal plane detector was a hexagonal close-packed array of 109 photomultiplier tubes (pmts) consisting of an inner region made up of 91 Hamamatsu R1398, UV glass tubes arranged in a hexagonal grid with 0.25° spacing. Each of these tubes had a photocathode diameter of 2.5 cm and viewed a 0.197° region of the sky. The outer ring consisted of 18 RCA 6342/IV tubes, each with a 4.27 cm diameter photocathode, and with a field of view of 0.336°. The 1995/96 data were gathered with a similar camera, differing in that the outer ring also consisted of 2.5 cm diameter tubes and light cones were used to increase the effective area of all 109 pmts. Each pmt was ac-coupled into an amplifier which fanned out the individual analog signals to a separate CAMAC analog-to-digital converter (adc) and a discriminator. When the telescope was triggered, the signal pulse from each of the 109 tubes was integrated for 25 nanoseconds,
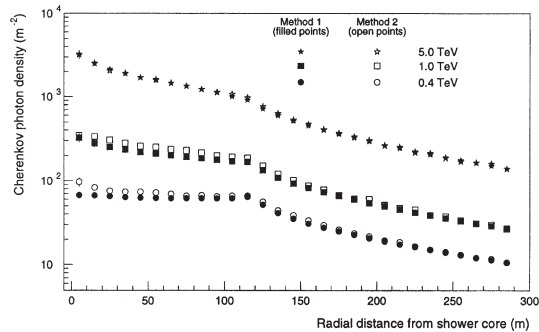
Fig. 1. Lateral distributions of the Cherenkov light from simulated, vertically incident showers at different energies, from the Method 1 simulations. Standard atmospheric absorption has been included for the Cherenkov photons, but their detection efficiency is not taken into account.

digitized and stored as digital units, "du". The overall gain of the pmts/amplifier/adc system is discussed in Section 2.3. A telescope trigger occurred when 2 of the inner 91 tubes simultaneously crossed a discriminator threshold which corresponded to about 50 du.

Each image recorded by the 10-meter telescope consisted of 109 values corresponding to the number of du registered in each pmt. The normalization of the relative gains of the individual pmts (flat-fielding) was done using images recorded nightly from a nitrogen flash lamp which uniformly illuminated the camera. Noise reduction in the images (image cleaning) was achieved by a morphological cleaning algorithm that used a bi-level threshold. Standard procedures for these have been described by Reynolds et al. (1993) and by Fegan (1996). After cleaning, each image was characterized by parameters (Hillas, 1985) which can be written in terms of first and second-order moments. Fig. 2 shows a geometrical representation of the parameters. The shape parameters, *width* and *length* combined with the orientation parameter, *alpha*, have proven very useful in selecting gamma-ray images from cosmic-ray background images. Other important parameters are the displacement of the centroid from the center of the field of view, *distance*, and the *size* (the total number of du) of the image. Both analyses described in this paper make use of only these five parameters. For taking data suitable for determination of spectra, the telescope was operated in the on-source/off-source mode in which the source was tracked for a given length of time, usually 28 sidereal minutes. Then the reflector was slewed back to track a background region covering the same range of elevation and azimuth as in the on-source run. All data used in this work were taken in this operating mode.

2.3. Telescope gain

The single most important parameter for extracting energy spectra is the overall telescope gain, which relates the energy of the primary gamma-ray to the *size* of the image. In this section, we estimate an absolute value for the overall gain by two different methods: (i) direct measurements, (ii) calibration using cosmic ray showers, and show that they give results in good agreement. In addition, we describe a scaling method that can be used to compare the overall gain for different observing seasons.

The fraction of the emitted Cherenkov light that is detected on average, depends on the following multiplicative factors:

(i) The absorption of the Cherenkov light by the atmosphere. This is not directly measured by us, and is also not well known at ultraviolet wavelengths. While an average attenuation is used in the simulations, it has been assumed that variable factors such as aerosols and high cirrus are unimportant. Some justification for this can be found in the fact that data taken under good weather conditions show very little night-to-night variations in the rate of Cherenkov triggers.
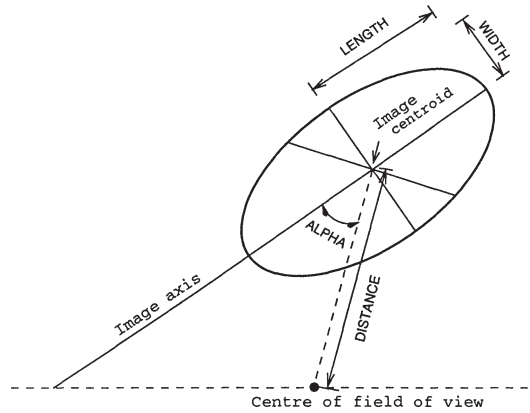
Fig. 2. Geometrical interpretation of the image parameters.

(ii) The reflectivity of the mirrors. This is not very well known as unprotected mirrors tend to degrade from exposure to the weather. For the original front-surfaced mirrors used in 1988/89, we have tried to estimate the degradation rate from the background cosmic-ray trigger rates. For this database which was taken over approximately a six-month period starting with freshly coated mirrors, we estimated that the average reflectivity was 15% lower than the manufacturer's specification. For the 1995/96 season, different mirrors were in place for which direct reflectivity measurements were made by the ARTEMIS group (Urban et al., 1996). The anodized aluminium coating on these mirrors make them less susceptible to weathering effects.

(iii) The quantum efficiency of the pmts. In Method 1, these are taken from the manufacturer's specification while Method 2 uses direct measurements made on a small subset of the pmts.

(iv) The combined gain of the pmts/cables/amplifier/adc system. The signal from each pmt is transmitted to the electronics through a considerable length of coaxial cable. The signal is also amplified by a factor of ten before the pulse is integrated by an adc. Some error is also introduced in the integration process due to straggling of pulses relative to the adc gate and variations in the pulse width. All of these are usually lumped into the single pe/du factor which relates photoelectrons produced by the pmts to du recorded in the image. Biller et al. (1995) have described various ways of measuring this factor, and as described below, our numbers are in good agreement with their values.

Combined together, the last three factors represent the overall gain of the telescope, the determination of which has been the focus of much of the work in extracting spectra.

There is a basic difference in philosophy between the two methods in determining the overall telescope gain. In Method 2 (cluster or ellipsoidal-window), the Monte Carlo simulation programs are used to calculate the cosmic-ray initiated trigger rate of the telescope. These simulated rates are then compared with the measured rates from data in order to estimate the overall gain of the telescope. This has the advantage that only a single measurement of the background trigger rate is required, but the disadvantage that it depends on correctly simulating the complex nuclear physics of an hadronic air shower, and on accurate measurements of the proton and alpha-particle spectra in this energy regime. In Method 1 (extended supercuts), direct measurements of the telescope characteristics are used where available, e.g., for the mirror reflectivity, cable losses, etc. This makes each measurement relatively straightforward but has the disadvantage that the overall factor depends on several measurements and there is one factor that is not measured directly – the atmospheric transmission. For the simulations used in Method 1, this was taken from the handbook compiled by Jursa (1985).

2.3.1. Direct measurements

In Method 1, an absolute calibration of the overall telescope gain was obtained from direct measurements. The pe/du factor for 1988/89 was measured by Kwok (1989) to be 1.15 ± 0.15 photoelectrons per du. This involved the measurement of two factors: (i) the current gain of the pmts using a light emitting diode (LED) as the light source and (ii) the amplification of the cables/amplifier system, using a radioactive alpha-emitter attached to a pmt that was hooked up to the electronics with and without the intermediate cabling. The pe/du factor is derived by averaging over a sample of several pmts. For the 1995/96 detector this factor was measured directly by Zweerink (1997) using essentially the same method as Kwok, and he obtained a value of 1.05 ± 0.10 photoelectrons per du. As a further check, proton simulations were done using the directly measured values for the overall gain as inputs to the Method 1 simulation programs. These were then compared with the background trigger rates and parameter distributions, and found to be consistent (Mohanty, 1997).

2.3.2. Calibration using cosmic ray showers

Method 2 carried out an absolute calibration of the overall telescope gain using the flux of background cosmic-rays. The spectrum of shower *sizes* produced by the known flux of cosmic-ray protons, helium and heavier nuclei was simulated, using the supposed light-conversion efficiencies and atmospheric transmittivity but leaving the number of photoelectrons per du as an adjustable parameter, and compared with the *size* spectrum in the off-source files from the 1988/89 Whipple Crab Nebula database. The energies of the simulated cosmic-ray particles were chosen so as to match the cosmic-ray fluxes in the range of 0.3 TeV to 100 TeV, with impact radii distributed uniformly in a circle of radius 313 m around the telescope. The shower origins were spread uniformly out to $3°$ from the center of the field, which was adequate provided that both simulated and observed images were restricted to certain ranges of the image parameters: $0.4°$ to $0.8°$ for *distance*, $0°$ to $0.75°$ for *length*, and $0.05°$ to $0.35°$ for *width*.

Fig. 3 compares the observed cosmic-ray *size* spectrum to the simulated spectrum, using integral spectra as is usual for scale comparisons. The best agreement is obtained by assuming a gain factor of 1.33 ± 0.06 photoelectrons per du, and the sensitivity may be judged by the much worse fit exhibited with a gain factor of 1.50. This calibration depends strongly on the proton flux at a few TeV, which is probably known no better than 15%. The helium flux is more accurately measured, and though uncertainties in the flux of heavier nuclei of several TeV are greater (see Fig. A.1), these are relatively unimportant as with the cosmic ray fluxes shown in the appendix, 59% of hadronic triggers of a typical size were due to protons, 26% to helium, and 14% to heavier nuclei. Incorporating an uncertainty of $\sim 16\%$ in the cosmic ray fluxes leads to a systematic uncertainty of 13% in the deduced gain factor, as the integral spectrum in Fig. 3 is described roughly by a power law with a slope of -1.25. Thus, from this method the gain factor is deduced to be 1.33 ± 0.18 photoelectron per du, including both statistical and systematic uncertainties.

This compares well with the laboratory value of 1.15 ± 0.15 obtained by Kwok (1989) and used in Method 1. As noted earlier, there are small differences in the assumed mirror reflectivity, PMT quantum efficiency and atmospheric transmission factors between the two methods, which could well account for the small difference in the deduced photoelectron to du conversion factor. Method 2 uses the efficiencies described in Rovero et al. (1996) and the atmospheric transmittivity derived for the UV-sensitive ARTEMIS (Urban et al., 1996) experiment.

2.3.3. Scaling techniques

We describe here a method of scaling the overall telescope gain from one season to the next and compare the values thus obtained to the direct measurements. The method uses the integral triggering rates of background cosmic-ray showers. After flat-fielding of the camera has been done as discussed in Section 2.2, within each cosmic-ray background image the individual channels can be ordered by the number of du recorded: the highest channel, second highest,... and so on. Ignoring the effects of fluctuations in pulse shape, the telescope trigger
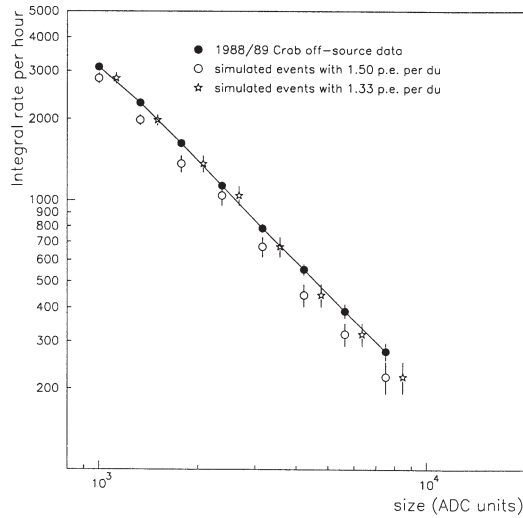
Fig. 3. Predicted and observed *size* spectrum for background cosmic-ray images, selected as described in the text. A conversion factor of 1.33 photoelectrons per du gives best agreement between the predicted and observed event rates.

in the usual operating mode is determined by the pmt which had the second largest number of recorded du, counting only the inner 91 tubes. Thus, the integral spectra of the rates in the second highest channel are related to the integral rates of the cosmic-ray showers.

We have empirically found that the integral rates in the second highest pmt, as a function of the number of du, are well described by a power law with an index of -1.33: $N(> \mathrm{du}) = (\mathrm{constant}) \times (\mathrm{du})^{-1.33}$. This is illustrated in Fig. 4 which shows integral spectra [1] for the second highest tube from cosmic-ray background showers measured at the zenith for calibration data taken in the 1988/89 season and the 1995/96 season. The effect of the telescope trigger is seen in the roll-over at the lower end of the spectra, starting at about 70 du. At the high energy end, the effects of saturation in the channel start affecting the rates as is evident from the last two bins in the figure. However, in between these limits, the spectra are very accurately described by a power law. By sliding the fitted lines horizontally till they overlap, the ratio of the gains for the two seasons is found to be 1.6. This is an overall gain ratio incorporating mirror reflectivity, photocathode quantum efficiencies, pmt gains, etc.

A systematic error can arise in this method if there were significant changes in the detector hardware in between the two seasons being compared. For example, light-collecting cones which increase the effective area of each pmt were added to the camera between 1988/89 and 1995/96. If there is structure in the shower image on a scale length comparable to the size of a pmt, the increase in the light collected in an individual pmt will not be proportional to the increase in effective area. This problem is somewhat alleviated by the fact that cosmic-ray images are rather broad and that the scaling is done between averages of a large number of shower images falling at random positions in the camera. Though such systematic effects are possible, it should be noted that statistical errors in the scaling may be made as small as desired simply by using more zenith calibration data.

The value for the telescope gain obtained by scaling can also be compared to the values obtained by direct measurements as described in Section 2.3.1. From the scaling techniques described above, we estimate that the overall gain of the telescope increased by a factor of 1.6 from the 1988/89 season to the 1995/96 season, where we have taken into account the fact that the triggering tubes in the 1995/96 camera occupied a 7%

---

[1] The spectral index of -1.33 differs from the -1.65 cosmic-ray spectral index because of the relationship connecting Cherenkov light content in a hadronic shower to the energy of the primary cosmic ray. See Mohanty (1995).
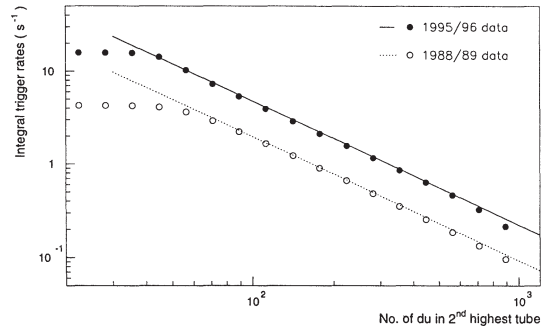
Fig. 4. Triggering rates of background cosmic-ray showers in 2nd highest tube, out of the inner 91. The figure shows both the observed rated (points) and the fits in the power-law regime (lines). Flat-fielding of the camera has been done, but the images are not cleaned.

larger area, by scaling down the 1995/96 rates by the same factor. The mirror reflectivity is known to have increased by a factor of about 1.2. The increase in the gain due to the addition of light-collecting cones for the 1995/96 season is calculated to be about 1.25 from the trigger rates for background cosmic-ray showers in zenith calibration runs taken on the same night, with and without the cones. Putting these factors together gives us $1.2 \times 1.25 = 1.5$. The remaining factor of $1.6/1.5 = 1.07$ can be attributed to a change in the pe/du factor, i.e., a change in the amount of direct amplification of the pmt signals. Thus, starting with the value of 1.15 photoelectrons per du for the 1988/89 season, the corresponding pe/du factor for 1995/96 would be $1.15/1.07 = 1.07$ photoelectrons per du which is in good agreement with the value of 1.05 ± 0.10 photoelectrons per du, obtained from the direct measurement described earlier. More details of the calculation using the scaling technique can be found in Mohanty (1997).

The two methods of telescope gain calibration are thus in good agreement, and the scaling technique further demonstrates the reliability of using the trigger rate of background cosmic rays as a measure of the efficiency of the detector. The photoelectron to du conversion factor derived here can be compared to other measurements of this factor. For the 1995/96 Crab database, we are in good agreement with the Biller et al. (1995) estimates that were roughly contemporaneous. Recently, the use of muon rings to calibrate atmospheric Cherenkov detectors has become popular. Rovero et al. (1996) have investigated this for the 1995/96 Whipple camera and obtain a photoelectron to du conversion factor that is about 20% different from ours. We believe that this level of disagreement is not surprising, given the muon ring technique presents several difficulties that are still being investigated. For example, the Cherenkov light from local muons explores a significantly different part of the spectrum as compared to that from air showers, with consequent differences in atmospheric transmittivity, mirror reflectivity, etc. Further, muon ring images are close to the trigger threshold and there can be significant loss of light due to the gaps in the spacing of the pmts, thereby making the calibration more dependent on proper image cleaning and on accurate modelling of the mirror aberrations, light cones, etc.

2.4. Simulations

In this work, two independent sets of Monte Carlo simulation programs have been used to model both shower development and the response of the Whipple 10m telescope. Method 1 uses a modified version of the KASCADE system (Kertzman and Sembroski, 1994) to simulate the development of atmospheric cascades, while Method 2 uses the MOCCA92 code (Hillas, 1995) for the same purpose. In both simulation programs, the paths of individual Cherenkov photons are ray-traced through the telescope optics.

Although the basic physics of the simulation programs (pair production, bremsstrahlung, multiple scattering, atmospheric absorption, etc.) is certainly understood, details of the models of some physical processes differ in the programs. For instance, there are differences in the treatment of the multiple scattering of electrons
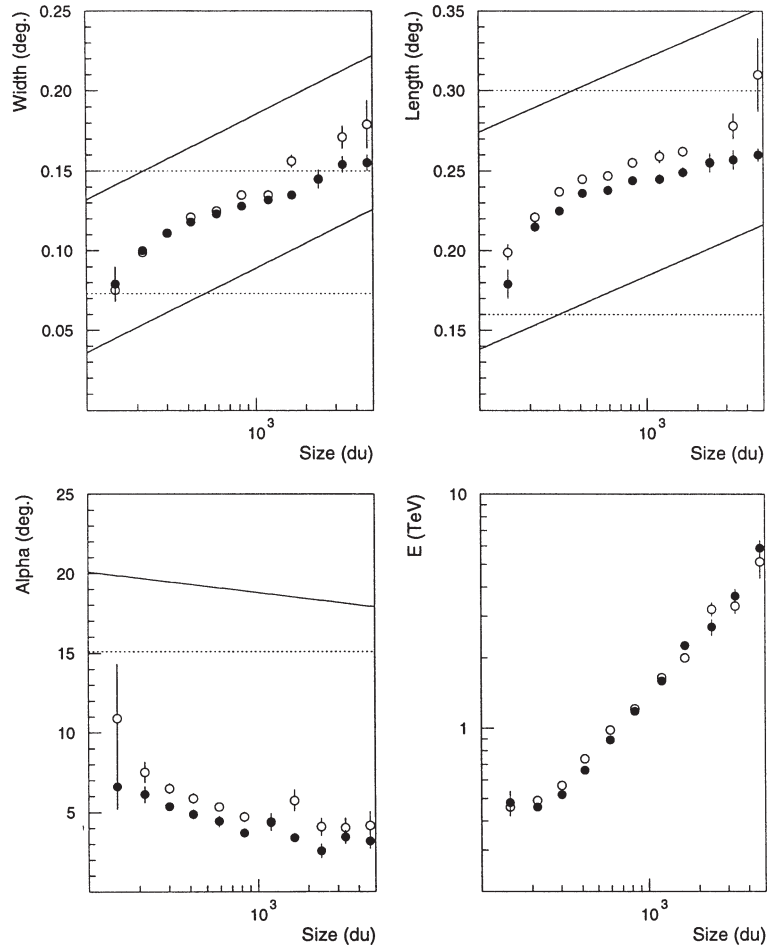
Fig. 5. A comparison of the mean shower parameters from the Method 1 (open circles) and Method 2 (solid circles) simulation sets is shown above. The parameters are binned by the image *size*. The dotted lines indicate the "supercuts" ranges described in Section 2.5.1 and the solid lines indicate the "extended supercuts" ranges described in Section 2.5.2.

in the shower, and of optical aberrations in the 10 meter reflector. Also, the two methods use quite different approaches for determining the overall telescope gain, though the final values are in quite good agreement. In some instances, such as in dealing with atmospheric absorption of Cherenkov light, these differences reflect uncertainties in our knowledge. We regard these variations in the programs as a strength, in that small differences in the modelling of physical processes seem not to be unduly influential in extraction of spectra.

Several sets of Monte Carlo simulations have been generated in which the number of gamma-rays is distributed in energy according to $\alpha E^{-\gamma}$ for various spectral indices γ. This makes it possible to cross-check methods by using one of the databases as a "reference" to obtain the detector characteristics relevant for spectral determination and using these characteristics to extract the spectral index from an independent database. The average elevation of the Crab for these observations was about 70°, so that this work makes use of gamma-ray showers simulated at that elevation.

Fig. 5 compares a sample of Method 1 and Method 2 simulations for gamma-ray shower parameters that are relevant for extraction of the Crab energy spectrum. The details of the simulations are as follows. The telescope was placed at an altitude of 2.3 km (the Whipple Observatory altitude), and it was assumed that the incidence

angle for the primary particle was 20° from the vertical. A minimum of 50 du was required in at least 2 of the inner 91 photomultiplier tubes, which is a crude model of the telescope trigger. Both simulation sets had a power-law energy spectrum with a differential index of approximately 2.4, with about 1500 simulated events passing the trigger condition in each set. The image parameters are then binned by $\ln(size)$. The mean and its 1σ error are shown for the parameters *width, length* and *alpha*. Also shown is the scaling of the simulated primary energy with the simulated shower *size*. The image parameters, *width, length, alpha*, and *distance* are the basis for distinguishing gamma-ray events from the cosmic-ray background. As can be seen from the figure, the Monte Carlo results agree reasonably well. The disagreements could well arise from the differences in the simulations that were discussed above.

2.5. Strategies for rejection of the cosmic-ray background

At gamma-ray primary energies above a few hundred GeV, the imaging technique works well in distinguishing between gamma-ray and cosmic-ray showers. In comparison with cosmic-ray images, gamma-ray images are more compact (i.e., have a smaller *width* and *length*), more uniform and have principal axes which point toward the source at the center of the field of view of the telescope (i.e., small *alpha*). Several selection strategies have been developed to exploit these differences: some of them are discussed here. The factor Q defined below is useful in measuring the effectiveness of gamma-selection methods:

$$Q = \frac{\text{Fraction of gamma-ray showers passing selection}}{\sqrt{\text{Fraction of background showers passing selection}}}. \tag{1}$$

In the limit of low signal-to-background ratio, background fluctuations are the dominant source of statistical uncertainty and Q is the factor by which imaging selection enhances a signal, i.e., a 5σ signal in the unprocessed data becomes a $5Q\sigma$ signal after image selection. One must be careful in comparing Q for different telescopes in that the mode in which the telescope is triggered may already preferentially select gamma-rays.

2.5.1. Supercuts gamma-ray image selection criteria

Gamma-ray images have *width, length*, and *alpha* parameters that fall into relatively narrow ranges of values. For the standard "supercuts" analysis, the range of each parameter was originally adjusted to optimize the significance of the Crab signal in the 1988/89 data (Punch et al., 1991). These ranges are

$$0.073 < width < 0.15,$$
$$0.16 < length < 0.30,$$
$$alpha < 15.1,$$
$$0.51 < distance < 1.1. \tag{2}$$

At present, the standard procedure selects only images with each of the four parameter values falling in the corresponding range [2]. The resulting Q is typically about 4. There are disadvantages in using this approach directly for the extraction of spectra because *width* and *length* grow with the primary gamma-ray energy. A simple remedy would be to scale the upper and lower boundaries for each parameter with the energy of the primary gamma-ray. This energy is, of course, not known. However, the *size* of an image provides an estimate of the primary energy, and the *width* and *length* are also well correlated with the logarithm of the *size*. The parameter means for *length, width* and *alpha* are accurately reproduced by a first-order polynomial fit in the variable $\ln(size)$. We have modified the supercuts procedure so that images with *width, length* and *alpha* parameters in a symmetrical range about their mean are accepted as candidate gamma-ray images. This set of selection criteria is called "extended supercuts".

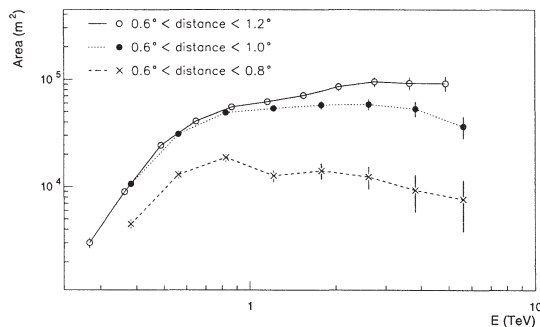[2] The ranges depend somewhat on the camera configuration which has changed with time.

Fig. 6. The collection area is plotted as a function of the primary energy for several different values of the upper bound in the parameter, *distance*. In each case, the lower bound in *distance* was 0.6°. Besides the selection in *distance*, no other cuts have been applied.

2.5.2. Extended supercuts gamma-ray image selection criteria

Extended supercuts form the basis of gamma-ray selection criteria employed in Method 1. Parameter ranges are chosen so that a large fraction (e.g., 95%) of simulated gamma-ray images are accepted by the selection mechanism. In order to arrive at suitable boundaries for the *length, width, alpha* and *distance* parameters, we used the Method 1 simulations where the primary gamma-ray has an energy drawn from a power-law spectrum with a differential spectral index of 2.4 and is incident at a zenith angle of 20°. The simulated showers were located randomly in an area extending to a radius of 250 meters from the telescope. If two of the 91 inner photomultiplier tubes exceeded 50 du, the telescope was triggered. Of the 54421 simulated events, 1691 triggered the telescope. Since the telescope trigger was not carefully modeled, the simulations may not be reliable near or below threshold (about 500 GeV) and only events above this energy were used in determining the spectra.

The extended supercuts selection criteria are based on *length, width, alpha* and *distance*. The image *distance* is not effective in distinguishing gamma-ray events from cosmic-ray events, but, if *distance* is not restricted the energy resolution of the telescope can be adversely affected. On the other hand, the collection area falls rapidly as the range of possible *distance* values is restricted. This is illustrated by the collection areas [3] shown in Fig. 6 for upper *distance* limits of 0.8°, 1.0° and 1.2°. The energy dependence of the collection area will be discussed more formally in Section 2.6. No other selection criteria have been applied, besides the cut in *distance*. In view of the trade-off between collection area and detector resolution, we have restricted *distance* to the range of 0.6° to 1.0° for both data and simulations. As indicated in Fig. 5, the *width* and *length* grow with energy. To derive the ranges for extended supercuts we proceeded as follows. For each of the three parameters (*width, length*, and *alpha*) used in the selection, the values for simulated showers that trigger the model detector were binned by ln(*size*). The parameter mean and its error were calculated for each bin. The means were then fit by a first-order polynomial ln(*size*), which is a good single-parameter estimator of the shower energy. A symmetrical range about the mean values was derived so that 95% of the simulated gamma-ray images passed each of the selections. These passbands are given below,

$$|width + 0.022 - 0.023\ln(size)| < 0.048 \,,$$
$$|length - 0.114 - 0.020\ln(size)| < 0.068 \,,$$
$$alpha - 9.16 + 0.558\ln(size) < 13.5 \,. \tag{3}$$

An advantage of having distinct parameters which can be used to select gamma-ray images is that they can be used separately or in combination. By selecting on the other parameters, one can produce a single-parameter

---

[3] Following convention, these are collection areas in a plane perpendicular to the optic axis of the telescope.

distribution that allows comparisons between simulations and data. For instance, the *width* and *length* can be used in combination to select gamma-ray-like events, and the resulting *alpha* values from the data can be histogrammed. By subtracting the off-source histogram from the on-source histogram, a distribution of *alpha* values for the excess is found. In practice, for finding the distribution for the shape parameters, *width* and *length*, we select only on *distance* and the orientation parameter, *alpha*. Conversely, the distribution of the orientation parameter, *alpha*, is found after selecting on *distance* and the shape parameters. This removes distortions that might arise due to correlations between the displayed parameter and the one on which the selection was made. An upper limit of $1.0°$ in *distance* is always used so as to avoid distorted images at the edges of the camera field of view.

Fig. 7 compares the distributions for *width, length* and *alpha*, selected as described above. Each of the leftmost three columns show the three different bands in *size*, while the rightmost column shows all selected events regardless of their *size*. The points in the figure represent difference histograms from the Crab 1988/89 database, while the solid lines show the Method 1 simulations. In every case the total number of events in the simulations have been renormalized to that in the data to facilitate the comparison. For the parameter *alpha* this renormalization is done only for the total number of events within the "signal" region: $alpha \leq 16°$. For clarity, we have combined in quadrature the $1 - \sigma$ error bars from the data and simulations, and shown these only on the data points. The errors in the simulations are approximately equal to those in the data. There is reasonable agreement between the data and the simulations in all *size* bands. However, focusing on the distributions for all selected events in the rightmost column, it can be seen that the simulated *alpha* distributions are about $4°$ narrower than the data and the simulated *width* distributions are about $0.01°$ narrower. To compensate for this, the *alpha*-boundary for the selection of gamma-ray events was increased by $4°$. This increase is taken into account in the boundary value of $13.5°$ given in Eq. (3). These discrepancies are largely due to telescope pointing errors that were not known well enough to be included in the simulations, as the observed *alpha* distribution was considerably narrower in 1995/96 when the telescope drive had been upgraded. If all three criteria were used to select gamma-ray-like images, the simulations indicated that 90% of the gamma-ray showers which triggered the telescope would be retained.

2.5.3. Cluster analysis: ellipsoidal-window gamma-ray image selection criteria

A cluster analysis, involving an ellipsoidal window, forms the basis of gamma-ray selection in Method 2. To describe this alternative method of image selection, it is convenient to refer to Fig. 8 which illustrates the use of parameter space to select gamma-ray images. The *length* and *width* of simulated gamma showers are shown by circles, while those of background showers, taken from real data, are shown by stars. (Only images restricted to $alpha < 18°$ and $0.5° < distance < 0.95°$ are included.) With a realistic source strength the proportion of gamma images would be much less than shown here, but even so, it is clear that a compact ellipsoidal region can be delineated in the parameter space, within which images are to be accepted. The ellipses indicated in Fig. 8 show these regions in the *length–width* plane for two values of *distance*, which may thus be regarded as being the axis normal to the page. This image selection method has several advantages. Firstly, by admitting a smaller region of parameter space, it more efficiently includes gamma-ray showers than the equivalent rectangular acceptance window used by standard supercuts, especially since some of the parameter variations are correlated. This leads to a higher *Q*-factor for the ellipsoidal-window method, as compared to either standard or extended supercuts. Secondly, a very simple mathematical prescription of cluster analysis exists to define such an ellipsoid from the statistical properties of a large sample of simulated images. This consists in using the Mahalonobis distance of a point in parameter space from the center of the "gamma-ray cluster" of points in that space. Therefore, there is actually a family of ellipsoids that differ only by their "radius" in a multi-dimensional parameter space. This is convenient, as the radius of the enclosing ellipsoid is the single parameter that needs to be optimized for a given dataset. The selection window is defined as follows. Given an image with original parameters $p_1, \ldots, p_4$, one first notes the deviation, q_i, of each parameter from
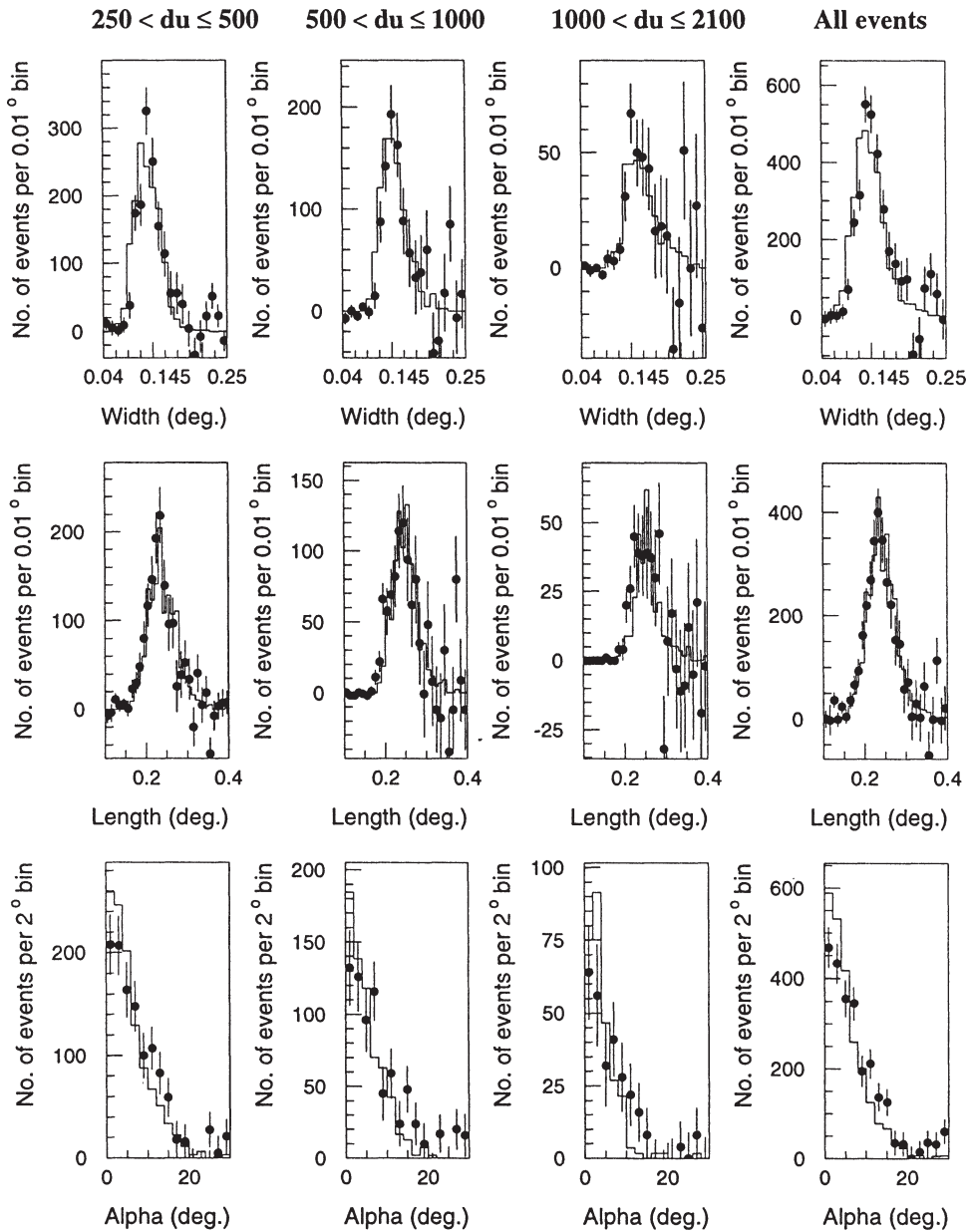
Fig. 7. A comparison of the parameter distributions from the 1988/89 Crab data (points) with those from the ISU simulations (solid lines) is given above for the parameters, *width, length* and *alpha*. This is done separately in each of three *size* bands and then globally for all selected events, with each column representing one set of comparisons as labelled at the top. In every case, the simulated distributions are renormalized to give the same total number of events as in the data. The data points were found by subtracting the off-source histograms from the on-source histograms. The error bars shown on the data points represent the errors from the data and the simulations, added in quadrature. Further details, including a description of the selection criteria used in obtaining the distributions, may be found in the text.
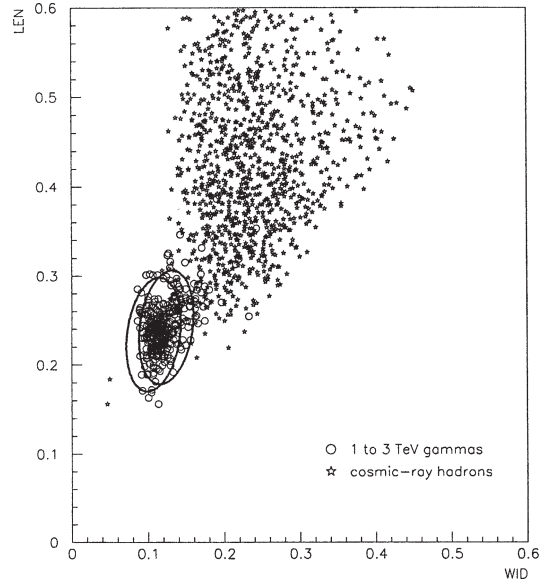
Fig. 8. The use of image parameters to select gamma-like images in the ellipsoidal-window selection technique is illustrated by showing the *width* and *length* of simulated gamma-ray images (circles) and of observed background showers (stars). Both distributions are in the *size* range of 499–999 du, corresponding to a gamma-ray primary energy of about 1 Tev. The curves are sections through an elliptical acceptance window with squared-radius, $d^2 = 5$, at two values of *distance*, chosen to be 1σ away on either side of the mean value.

the mean value expected for gamma-ray images,

$$q_i = p_i - \langle p_i \rangle . \tag{4}$$

Then, the Mahalonobis distance d of the image point from the center of the cluster is given by

$$d^2 = \sum_{i=1}^{4} \sum_{j=1}^{4} M_{ij} q_i q_j , \tag{5}$$

where the matrix M_{ij} defining the metric of this parameter space is simply the inverse of the second moment (or covariance) matrix,

$$C_{ij} = \sigma_{ij} = \langle q_i q_j \rangle . \tag{6}$$

In the simple case of uncorrelated parameters where C_{ij} and M_{ij} have only diagonal terms, this is equivalent to $d^2 = \sum (q_i^2/\sigma_{ii})$, and for four parameters the mean value of d^2 would be 4. For purely Gaussian distributions in four dimensions, only about 60% of the events would lie within a radius of $d^2_{max} = 4$, so, in practice, windows defined by d^2_{max} in the range 6 to 10 have been used. Fig. 9 shows how the acceptance changes with d^2_{max}. The lines in the figure represent the increase in the number of accepted gamma-ray images with increasing d^2_{max}, as predicted by the Method 2 simulations. The points are the excess number of selected images in the on-source region over the number in the off-source region, from the 1988/89 Crab Nebula database. Different sets of lines and points are indicated for each of four different *size* bands. It can be seen that it would be unwise to use a small window ($d^2_{max} < 5$, say), as in this region the acceptance varies rapidly with d^2_{max} and, hence, the result would be unduly sensitive to errors in the simulation. Too large a window, on the other hand, admits too many background showers, thereby reducing the Q-factor. Therefore, the practice has been to deduce spectra by comparing the excess numbers with the predicted curve for values of d^2_{max} between 6 and 10. Two further
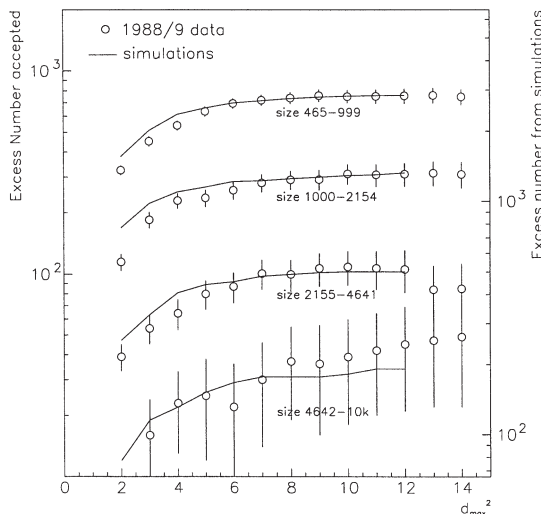
Fig. 9. The number of images within an ellipsoidal window is shown above as a function of the square of the window radius, expressed as a Mahalonobis distance. The parameters used are *distance, width, length* and *alpha*. The four curves correspond to the four logarithmic bands in the image *size* that are actually used for the spectrum estimation (see Table 3). These size bands, from top to bottom, are: 455–999, 1000–2154, 2155–4641, 4642–9999. The points are from the 1988/89 database and the curves are from the Method 2 simulations (the right-hand scale on the figure applies to these curves, assuming a gamma-ray spectrum given in Section 3.2).

refinements of the technique should be mentioned. Firstly, the parameter *alpha* has a one-sided distribution peaked at zero, so that the deviation from zero is appropriate rather than from the mean value. To allow for this, we have set the mean, variance and covariances of the parameter, *alpha*, to,

$$\langle alpha \rangle = 0 \,, \qquad \sigma_{ii} = \langle (alpha)^2 \rangle \,, \qquad \sigma_{ij} = 0 \,, \tag{7}$$

respectively. Secondly, the matrix M_{ij}, defining the metric of the parameter space, is determined separately for images in several distinct *size* bands, so as to allow for an energy-dependence in the image characteristics.

A further adjustment was needed in the 1988/89 season, where because of the telescope pointing errors already mentioned, it was necessary to add $8°$ in quadrature to the predicted r.m.s. spread of *alpha*, so as to bring it into agreement with the observed spread. Ignorance of the detailed characteristics of the varying small pointing errors made it impossible to model the effect on *alpha* more accurately than this.

2.6. Collection area and energy threshold

In order to convert the observed rate of gamma-ray showers to a flux from the source, one needs to know the effective area on the ground over which the detected showers are distributed. This effective collection area at a particular energy can be calculated by simulating gamma-ray showers falling at random positions over a sufficiently large area [4], A_0, and recording the number of shower images which trigger the telescope and pass the selection criteria. The area at an energy, E, is then given by

$$A(E) = A_0 \left(\frac{\text{number passing selection at } E}{\text{number simulated at } E} \right) . \tag{8}$$

---

[4] For the purpose of this work, a circle of radius 250 m proves easily adequate. Note also that, as per usual practice, all such areas are defined in a plane perpendicular to the optic axis of the telescope.

The general shape of the collection area has been shown in Fig. 6. For a reasonable allowed range in the parameter *distance*, the area curve rises rapidly at low energies and falls off more gradually at high energies. The collection area goes to zero at low energies because very low energy showers do not produce enough light intensity to trigger the telescope. At high energies, the area is limited by the upper bound on the *distance* parameter, which is imposed in order to improve the energy resolution. From reference to Fig. 1 it is seen that the Cherenkov light intensity is closely related to the photon energy for showers with impact radii in the range of 40 m to 125 m from the detector. The imposed *distance* restriction of $0.6°$ to $1.0°$ selects showers in that range of impact radii, at least to a first approximation.

It is desirable that the collection area vary slowly with energy. At high energies, where most of the gamma-ray showers trigger the detector, the collection area is relatively stable against uncertainties in the simulations. Near the energy threshold, the area estimated from the simulations is unreliable as it is highly dependent on the triggering characteristics of the telescope. Uncertainties in the magnitude of $A(E)$ result in errors in the deduced flux, while uncertainties in the shape of $A(E)$ result in errors in the spectral index.

2.7. Energy estimation

The Cherenkov light intensity in an image (proportional to the *size* parameter) is the key to estimating the energy of the primary gamma-ray. As illustrated in Fig. 1, the light intensity is a good measure of the primary energy for showers with impact radii in the approximate range of 40 m to 125 m, with possibly a small correction applied for the actual impact radius. The region beyond the rim of the lateral distribution should be avoided altogether as the light intensity is strongly dependent on the (unknown) impact radius. Also, the shower-to-shower fluctuations in the light intensity become very large within about 30 m from the shower axis (Macomb, 1989), as most of the light in this region is produced by local, penetrating particles which can vary widely in their number. Thus, it is prudent to impose both upper and lower limits on the impact radius of the selected showers.

In practice, the impact radius is not directly measured. Instead, the angular *distance* of the image centroid from the source location in the field-of-view is used as an approximate measure of the impact radius, so that in order to reconstruct the primary energy from the *size* it becomes necessary to impose suitable upper and lower limits on the parameter *distance*. A *distance* range of $0.6°$ to $1.0°$, was found to give the desirable combination of fairly sharp energy estimates with sufficient collection area for Method 1. Method 2, which avoids making energy estimates for individual showers, was found to be tolerant of a slightly larger range in *distance*: $0.5°$ to $1.1°$. Both of these ranges include the peak of the *distance* distribution of the observed excess in the data.

In Method 1, the energy of each shower is explicitly estimated. A logarithmic energy variable proves useful here, so that we define $x, \tilde{x}$, to be the natural logarithm of the true energy, E, and of the estimated energy, $\widetilde{E}$, respectively. By fitting a large sample of simulated gamma-ray showers passing the selection criteria, we have found that a suitable energy estimate can be obtained by describing $\tilde{x}$ as a second-order polynomial in $\ln(size)$ and *distance*. The polynomial coefficients are chosen so as to simultaneously minimize both the mean-squared error, $\sum(x - \tilde{x})^2$, and the bias, $\sum(x - \tilde{x})$, in the estimated energy for a given true energy, for the events in each of several estimated energy ranges. To avoid distortions that arise below the trigger threshold, we have included only Monte Carlo events above a true energy of 250 GeV and obtain the energy estimate,

$$\tilde{x} = -8.11 + 2.56 \ln(size) - 9.25\, distance - 0.120[\ln(size)]^2$$
$$+ 6.26(distance)^2 + 0.0105 \ln(size) \cdot (distance)\,, \tag{9}$$

Fig. 10a shows the distribution of $x - \tilde{x} = \ln(E/\widetilde{E})$, binned by the primary energy, E. The bias is tolerable small in each energy range. Also, Fig. 10b shows the distribution of $x - \tilde{x} = \ln(E/\widetilde{E})$, which we refer to as the energy resolution function. For the 1988/89 observing season, with images selected by extended supercuts, this is well fit by a Gaussian with $\sigma = 0.36$. An energy estimate along these lines was originally
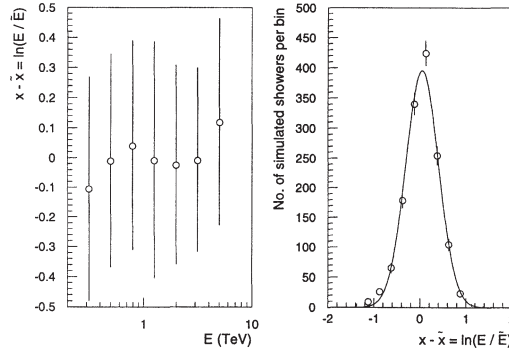
Fig. 10. (a) The error in the energy resolution, $x - \tilde{x} = \ln(E/\widetilde{E})$, is shown for several primary energy bins. (b) A histogram of the values of $x - \tilde{x}$ for all selected events is shown. The solid line is a Gaussian fit with a standard deviation of 0.36. The simulations are appropriate for the 1988/89 season, and all events have been selected by extended supercuts.

proposed by Plyasheshnikov and Konopelko (1989b), and our observed spreads are roughly compatible with their predictions. The non-intuitive form of the above energy estimate, containing strongly varying successive terms, where one would expect $\widetilde{E}$ to be almost directly proportional to the image *size*, was one of the principal reasons for introducing Method 2 as a check. In the latter method, energies are not estimated for individual showers. Instead, a postulated energy spectrum is adjusted until the resulting simulated *size* spectrum matches the *size* spectrum observed in the data. The relationship between *size, distance* and the primary energy is thus implicit in the simulations and requires no analytical approximation.

2.8. Energy resolution

The energy resolution function, as described above, is a Gaussian with $\sigma_x = 0.36$. The width of the resolution function determines the scale of the smallest structure that would be apparent in a histogram of estimated energies. An appropriate choice for the energy bin size is also obviously tied to the telescope resolution. If one wishes to be sensitive to narrow features in the spectrum the maximum bin size should be about $\Delta x = 2\sigma_x$, which would include most of the area in the peak. This choice would be appropriate for weak signals riding on top of a large background. In the other limit, where background is negligible, the bin size which minimizes the mean squared-error introduced by the binning, assuming Gaussian error distributions, has been shown by Scott (1979) to be

$$\Delta x = 2(9\pi)^{1/6}\sigma/n^{1/3} = 3.49\sigma/n^{1/3}, \tag{10}$$

where n is the number of data points in the histogram. This becomes less than $\sigma/2$ for $n \geq 340$ and decreases very slowly with n. With background present, the additional fluctuations would only increase the optimal value of Δx. Thus, in the present application, a suitable choice of energy bin size would be around σ_x, i.e., about six energy bins per decade.

2.9. Threshold energy

Although not of immediate relevance to the methodology of estimating energy spectra, the effective energy threshold of a Cherenkov telescope is nevertheless important for comparing the responses of different detectors to a given source stimulus and for the estimation of an absolute flux of gamma-rays above a pre-determined threshold energy, that can then be compared with other results.

Though there is not yet a general consensus in the field of TeV gamma-ray astronomy on a precise definition of the threshold energy, we have chosen to follow the prescription of Weekes (1976), and define a "traditional energy threshold" as the energy at which the differential event rate of the telescope would be peaked for a source having a power-law spectrum with an integral index of 1.6. The effective collection area is then defined in terms of an idealized detector with a collection area that is constant above the energy threshold, and zero below it. The effective area is taken to be the area that such an idealized detector would need to have in order to exhibit the same event triggering rate as the real detector, for a source with a 1.6 power-law index. It is prudent to avoid the region below the traditional energy threshold in determining energy spectra, because of difficulties in modelling the region close to the hardware trigger. We estimate that approximately 30% of the total number of observed events from the Crab are from gamma-ray showers with primary energy below this traditional threshold. The telescope threshold, as defined above, is estimated to be about 500 GeV for the 1988/89 detector, while the lowest energy detected was about 200 Gev. Thus, we believe this to be a conservative definition of the telescope threshold.

3. Determination of spectra: application to the Crab Nebula

This section describes two quite different approaches to spectral determination that yield results in agreement with each other. We focus mainly on the Whipple Crab database of observations from the 1988/89 season. This was chosen because it is large, uniform, and was taken just after the telescope mirrors had been freshly recoated, so that their reflectivity was high and relatively well known. It is uniform in that the triggering schemes and hardware setup were the same throughout the season with no updates or adjustments. This database has also been extensively studied (Vacanti et al., 1991; Punch et al., 1991) and was also the basis of an earlier analysis of the Crab spectrum (Vacanti et al., 1991). The intermediate results (expressions for collection area, estimated energies, etc.) presented are all derived from this dataset. We also give the final results for an analysis of the more recent 1995/96 database using Method 1. The camera used in 1995/96 differs in pmt positions and sizes, and in the use of light cones to enhance light collection efficiency. The methods described in Section 2.3 were used to ensure a consistent treatment of the two databases.

It is generally not possible, without unlimited statistics, to extract spectral features that are considerably smaller than the width of the energy resolution function. It has been standard to assume a simple power-law form for the source spectrum, viz.

$$S(E)\,dE = \alpha E^{-\gamma}\,dE\,, \tag{11}$$

where $S(E)\,dE$ is the number of gammas per unit area per unit time in the infinitesimal interval, dE, at an energy E. The spectra found for the Crab from analyses presented here are consistent with this simple form. In terms of the dimensionless logarithmic energy variable, x, the power-law spectrum, $R(x)$, is given by

$$R(x)\,dx = S(E)\,dE\,,$$

from which it follows that

$$R(x)\,dx = \alpha\,e^{(1-\gamma)x}\,dx\,. \tag{12}$$

3.0.1. Method 1: extraction of the spectrum

In Method 1, the extended supercuts technique (Section 2.5.2) is used to select gamma-ray images and for these images, an energy estimate ($\tilde{x}$) is made on the basis of *size* and *distance* (Section 2.7). The estimated energies are binned separately for the on-source and off-source runs, and the two histograms are subtracted. Thus, each bin contains the difference between on-source and off-source runs, accumulated over the entire observation season. The expected number of counts in a bin of width Δ, centered on $\tilde{x}_m$ is given by

$$\Phi(\tilde{x}_m) = T \int_{\tilde{x}_m-\Delta/2}^{\tilde{x}_m+\Delta/2} d\tilde{x} \int_{-\infty}^{\infty} A(x)\alpha\, e^{(l-\gamma)x}\psi(x \to \tilde{x})\, dx\,, \tag{13}$$

where T is the total on-source observation time, x is the logarithm of the real energy, $A(x)$ is the collection area, and $\psi(x \to \tilde{x})$ is the resolution function that maps x into $\tilde{x}$. By adjusting α and γ in Eq. (13), the binned data are fit via a χ^2 minimization procedure. This calculation can be further simplified by choosing a bin size in the estimated energy that is equal to the width of the resolution function (Section 2.8). Then, the expected number of counts in each estimated energy bin of size, Δ, is approximated by

$$\Phi(\tilde{x}_m) = T\Delta \int_{-\infty}^{\infty} A(x)\alpha e^{(l-\gamma)x}\psi(x \to \tilde{x}_m)\, dx\,. \tag{14}$$

This method is simple and direct, but has the disadvantage that the functional form of the spectrum must be known a priori – here a simple power law was assumed. For spectra which do not differ dramatically from a power law, it is possible to compute a "modified area" (Section 3.1.2) which includes the effect of the resolution function. Using this approach makes it possible to extract the flux as a function of energy and to detect spectral structure larger than the width of the resolution function.

The 1988/89 database consists of 52 ON/OFF pairs of runs, each approximately 28 minutes long. The total length of time on-source is 85 980 s, with the off-source region observed for the same time. After selection by the extended supercuts criteria, the excess counts, binned by the dimensionless logarithmic energy estimate, $\tilde{x} = \ln(\widetilde{E}/\text{TeV})$, are given in Table 1 below. The error in the excess counts for a given bin are derived by assuming Poissonian uncertainties in the observed number of on-source and off-source events in that bin. The collection area, A, and the modified collection area, $\widetilde{A}$, are also tabulated, as is the flux with 1σ errors. The modified collection area incorporates the effects of the telescope energy resolution and also allows us to extract spectral points that can be useful even if the spectrum departs from a power-law form. It is described in detail in Section 3.1.2. The best fit to the binned data was found by varying α and γ to minimize χ^2, yielding a value of $\chi^2_{\min} = 6.99$ for 6 degrees of freedom at $\alpha = 3.41 \times 10^{-7}$ and $\gamma = 2.38$, as given in Eq. (15). A contour plot of χ^2 is shown in Fig. 11, where the dot at the center is minimum. Each successive solid contour line represents an increase in χ^2 of one unit. The dashed contour line corresponds to $\chi^2 = \chi^2_{\min} + 2.3$ which is the 68% confidence level for α and γ (Avni, 1976; Lampton et al., 1976). The statistical errors given in Eq. (15) are the outer bounds of this ellipse. (A discussion of possible systematic errors is given later in Section 4.1.) The full set of calculations were then repeated using the Method 2 gamma-ray simulations with essentially the same resulting spectrum. The derived spectrum for the 1988/89 database is

$$S(E) = (3.41 \pm 0.25) \times 10^{-7} \left(\frac{E}{1\ \text{TeV}}\right)^{-2.38\pm0.10} \text{m}^{-2}\ \text{s}^{-1}\ \text{TeV}^{-1}\,. \tag{15}$$

The same procedure was then applied to the 1995/96 database with results given in Table 2. For 1995/96 the main change in the telescope hardware was the addition of light-collecting cones, which lowered the energy threshold and enhanced the telescope trigger rate for atmospheric Cherenkov showers but at the price of also increasing the noise arising from fluctuations in the night-sky brightness. The nature of the dominant component of the background changed from the Cherenkov light of cosmic-ray-initiated air showers to the light generated by penetrating single muons created in the particle cascades that happened to come close to the telescope. In order to reject muons and guard against spurious noise triggers we have chosen to artificially raise the telescope threshold by imposing a trigger requirement of 70 du in two out of the inner 91 tubes, rather than the 50 du in 2/91 used for the 1988/89 season. This requirement also rejects lower energy gamma-ray showers so that the collection area and the modified collection area for the two observing seasons, as given in Table 1 and Table 2 are not markedly different.

Table 1
Method 1 energy spectrum for the Whipple 1988/89 database

$\tilde{x}_{\text{mid.}}$	$\widetilde{E}_{\text{mid.}}$ (TeV)	$\Delta\widetilde{E}$ (TeV)	Excess counts	A (10^4)	$\widetilde{A}$ (10^4 m^2)	Flux $\pm 1\sigma$ error (m^{-2} s^{-1} TeV^{-1})
-0.576	0.562	0.217	577 ± 41	2.70	2.34	$(1.32 \pm 0.09) \times 10^{-6}$
-0.191	0.826	0.319	601 ± 44	4.50	4.10	$(5.34 \pm 0.39) \times 10^{-7}$
0.191	1.211	0.467	402 ± 38	5.10	5.29	$(1.89 \pm 0.18) \times 10^{-7}$
0.576	1.778	0.687	278 ± 31	5.24	5.72	$(8.23 \pm 0.92) \times 10^{-8}$
0.960	2.612	1.008	180 ± 24	5.31	5.66	$(3.66 \pm 0.49) \times 10^{-8}$
1.342	3.828	1.478	135 ± 20	4.64	5.20	$(2.04 \pm 0.30) \times 10^{-8}$
1.727	5.623	2.171	25 ± 16	3.24	4.19	$(3.19 \pm 2.04) \times 10^{-9}$
2.111	8.260	3.188	18 ± 7	2.00	2.75	$(2.39 \pm 0.93) \times 10^{-9}$

For each bin in the estimated energy, the excess counts, collection area and the flux are given. The flux is derived by dividing the excess counts by the product of the modified area, estimated energy bin size, and the observation time.

Table 2
Method 1 energy spectrum for the Whipple 1995/96 database

$\tilde{x}_{\text{mid.}}$	$\widetilde{E}_{\text{mid.}}$ (TeV)	$\Delta\widetilde{E}$ (TeV)	Excess counts	A (10^4)	$\widetilde{A}$ (10^4 m^2)	Flux $\pm 1\sigma$ error (m^{-2} s^{-1} TeV^{-1})
-0.576	0.562	0.217	683 ± 60	3.25	2.74	$(1.45 \pm 0.13) \times 10^{-6}$
-0.191	0.826	0.319	513 ± 50	4.77	4.36	$(4.66 \pm 0.45) \times 10^{-7}$
0.191	1.211	0.467	388 ± 40	4.95	5.40	$(1.94 \pm 0.20) \times 10^{-7}$
0.576	1.778	0.687	222 ± 33	5.00	5.72	$(7.13 \pm 1.06) \times 10^{-8}$
0.960	2.612	1.008	108 ± 26	5.04	5.59	$(2.42 \pm 0.58) \times 10^{-8}$
1.342	3.828	1.478	109 ± 24	4.63	5.25	$(1.77 \pm 0.39) \times 10^{-8}$
1.727	5.623	2.171	9 ± 17	3.81	4.77	$(1.10 \pm 2.07) \times 10^{-9}$
2.111	8.260	3.188	15 ± 8	2.71	4.17	$(1.42 \pm 0.76) \times 10^{-9}$

For each bin in the estimated energy, the excess counts, collection area and the flux are given. The flux is derived by dividing the excess counts by the product of the modified area, estimated energy bin size, and the observation time as described in Section 3.1.2. A trigger requirement of 70 du in two out of the inner 91 tubes has been imposed.
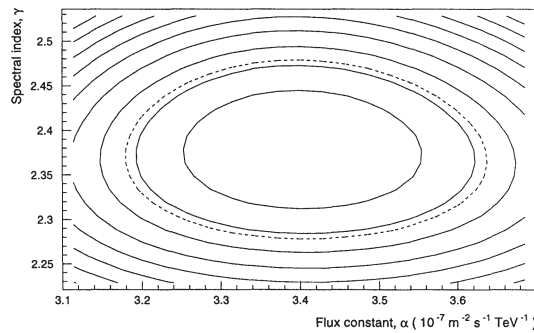

Fig. 11. Method 1: contours of χ^2 for the 1988/89 are shown. The dot at the center is the minimum value and χ^2 increases by one unit for each solid contour. The dashed-line contour represents the 68% confidence level region. Note that the ellipses are approximately aligned with the axes, implying that the errors in α and γ are approximately uncorrelated with the spectrum written in the form: $\alpha(E/\text{TeV})^{-\gamma}$.

The 1995/96 database consists of 49 ON/OFF run pairs, each approximately 28 minutes long, giving a total on-source observation time of 79 154 s and an equal amount of time off-source. The best-fit spectrum, with a value of $\chi^2_{\text{min}} = 7.02$ for 6 degrees of freedom, is given by

$$S(E) = (3.12 \pm 0.40) \times 10^{-7} \left(\frac{E}{1 \text{ TeV}} \right)^{-2.57 \pm 0.12} \text{ m}^{-2} \text{ s}^{-1} \text{ TeV}^{-1} . \tag{16}$$

A disadvantage of this simple fitting procedure is that the form of the spectrum must be assumed a priori and the only indication that the assumed form might be incorrect is a large value of χ^2.

3.0.2. Modified area and flux determination

The concept of a modified collection area is useful to allow a simple estimation of fluxes from putative gamma-ray sources. In effect this is an average of the collection area in a given energy bin, taking into account the effect of the source spectrum and the energy resolution of the detector. Also, it enables the calculation of useful fluxes even if the source spectrum does not follow a simple power law. For example, from a consideration of the fluxes measured from the Crab Nebula by other experiments at different energies, one would expect the spectrum to deviate from a simple power law at both the higher and the lower energies (Hillas et al., 1997). Such deviations are taken into account below by viewing the parameter γ as a function of the estimated energy.

Eq. (14) relates the observed number of counts to the source spectrum. It can be rewritten as

$$\Phi(\tilde{x}_m) = T \int_{\tilde{x}_m - \Delta/2}^{\tilde{x}_m + \Delta/2} R(\tilde{x}) \widetilde{A}(\tilde{x}) \, d\tilde{x}, \tag{17}$$

where $\widetilde{A}(\tilde{x})$ is the modified collection area given below,

$$\widetilde{A}(\tilde{x}) = \left[\int_{-\infty}^{\infty} R(x) A(x) \psi(x \to \tilde{x}) dx \right] / R(\tilde{x}) , \tag{18}$$

where $R(x)$ is the differential flux in terms of the dimensionless logarithmic energy variable, x (Section 3).

If the modified area were known, the flux in a bin of small width is given simply by

$$R(\tilde{x}_m) \cong \frac{\Phi(\tilde{x}_m)}{T \widetilde{A}(\tilde{x}_m) \Delta} . \tag{19}$$

Thus, the modified area includes the effect of the resolution function. It can be calculated by an iterative procedure:
 (i) initially assume that the resolution function is a delta function, i.e., $\widetilde{A}(\tilde{x}) = A(\tilde{x})$;
 (ii) next find the first approximation to the flux, $R_1(\tilde{x}_m)$, by fitting the data;
(iii) then recalculate $\widetilde{A}(\tilde{x})$ using the correct resolution function and $R_1(\tilde{x}_m)$.
Steps (ii) and (iii) can then be repeated until convergence, yielding successive approximations $R_n(\tilde{x}_m)$.

In Section 2.8, it was shown that the resolution function $\psi(x \to \tilde{x})$ is Gaussian to a good approximation, which simplifies the analysis. For a power-law spectrum, with $R(x)$ given by Eq. (12), $\widetilde{A}(\tilde{x})$ can be written as

$$\widetilde{A}(\tilde{x}) = \frac{e^{\sigma^2(1-\gamma)^2/2}}{\sigma \sqrt{2\pi}} \int_{-\infty}^{\infty} e^{-(x-\tilde{x}_0)^2/2\sigma^2} A(x) \, dx ,$$

$$\cong e^{\sigma^2(1-\gamma)^2/2} \left[A(\tilde{x}_0) + \frac{\sigma^2}{2} A''(\tilde{x}_0) + \cdots \right] , \tag{20}$$

where $\tilde{x}_0 = \tilde{x} - \sigma^2(\gamma - 1)$. If the resolution function is narrower than features in the collection area, its principal effect is to shift the point at which $A(x)$ is evaluated towards lower energies and to renormalize the overall
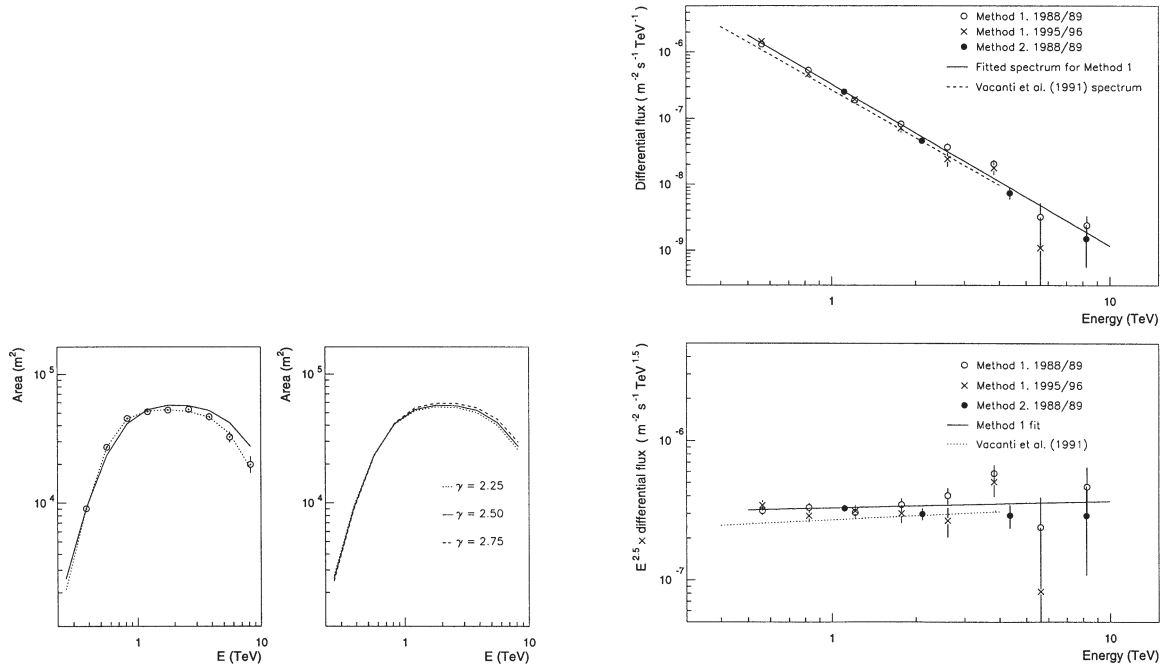
Fig. 12. In the left half of the figure, the points with errors show the collection area, A, as a function of the primary energy, for the 1988/89 database. The dotted line is the minimized χ^2 fit to the points, while the solid line shows the modified area (Section 3.1.2), $\widetilde{A}$, for a spectral index of $\gamma = 2.50$, close to the inferred spectral index for the Crab. The right half of the figure shows several $\widetilde{A}$ curves for different spectral indices: $\gamma = 2.25, 2.5, 2.75$. As can be seen, these are close to each other.

Fig. 13. The spectrum of the Crab Nebula in the TeV region. The solid line is at least-squares fit to the Method 1 fluxes for both seasons. The dashed line is the Vacanti et al. (1991) spectrum.

shape. In the left part of Fig. 12, the collection area for the 1988/89 Crab database is shown along with the modified area (solid line) and the corresponding numbers are given in Table 1. These were calculated assuming $\gamma = 2.5$, which is very close to the Crab spectral index. The width of the resolution function was assumed to be $\sigma = 0.36$, the value given earlier. The right half of the figure shows that the modified area is not sensitive to the precise values of γ in that the curves for $\gamma = 2.25, 2.5, 2.75$ are essentially the same. Thus the procedure of assuming a value for γ, extracting a spectrum and recalculating γ converges very rapidly – here in a single iteration. This approach would also reveal any change in the slope of the spectrum. The modified area was used to calculate fluxes for the Crab 1988/89 database and the results are plotted as crosses in Fig. 13. A least-squares fit to the fluxes yields $\chi^2_{min} = 7.82$ at $\gamma = 2.34$ and $\alpha = 3.34 \times 10^{-7}$ which is consistent with the results for 1988/89.

3.1. Method 2: extraction of the spectrum

Method 2 differs from Method 1 in two main respects. Firstly, the ellipsoidal-window selection technique (Section 2.5.3) is used to select gamma-ray images. Secondly, instead of going through the process of explicitly estimating the collection area, energy estimate, etc., a simpler approach is adopted for extracting the energy spectra. Both data and simulated gamma-ray showers are selected by the same criteria and binned by $\ln(size)$. The input energy spectrum to the Monte Carlo simulations is then adjusted till the simulated *size* spectrum matches the observations.

The simulated events were distributed randomly over a circular area in a plane perpendicular to the arrival

Table 3
Method 2: energy spectrum for the 1988/89 Whipple Crab Nebula database

size band	N (excess)	N (sim.)	Ratio	⟨E⟩ (TeV)	Flux at ⟨E⟩ and 1σ error (m⁻² s⁻¹ TeV⁻¹)
465–999	756 ± 45	4877	0.155	1.11	$(2.52 \pm 0.15) \times 10^{-7}$
1000–2154	297 ± 10	1980	0.150	2.11	$(4.60 \pm 0.46) \times 10^{-8}$
2155–4641	104 ± 18	662	0.157	4.36	$(7.32 \pm 1.39) \times 10^{-9}$
4642–9999	35 ± 22	209	0.167	8.22	$(1.50 \pm 0.94) \times 10^{-9}$

Excess counts are binned by *size* and compared with the results of simulations. The fluxes arrived at through Method 2 are given in column 6.

direction of the showers that extended out to a radius of 313 m, and covered an energy range from 0.31 TeV to 19 TeV. Weights were attached to the simulated events so that the overall weighted spectrum corresponded to $0.1E^{-1.6}$ gammas per m⁻² above an energy E TeV. The weights could then later be altered to represent any other trial spectrum, as is done in trying to match the observed *size* spectrum. Simulated gamma-ray shower images were required to pass a trigger requirement that at least two of the inner 91 channels exceed 80 du (a somewhat more conservative requirement than in Method 1), and were also selected by the ellipsoidal-window selection method. These events were then grouped by ln(*size*) in one-third decade bands, and for each band the parameter means and variances were used to derive the C_{ij} and M_{ij} matrices. These matrices were then used in the selection of gamma-ray-like images, with the data sorted into the same ln(*size*) bands.

The four size bands used were: 465–999, 1000–2154, 2155–4641, and 4642–9999 du. The Mahalonobis distance, d, of each event from the expected center of the gamma-ray cluster was calculated from Eq. (5) using the matrix for the appropriate *size* band. Fig. 9 shows the excess number of selected images in the on-source region over the number in the off-source region, plotted as a function of the square of the window-size, d^2_{max}, for each of these four *size* bands. The data come from 45 ON/OFF pairs from the 1988/89 Crab database where the mid-run zenith angle was in the range of 9.7° to 23.9°, so as to be close to the zenith angle of 20° used in the simulations. On the same figure, the lines indicate the number of gamma-rays predicted from the simulations (the right-hand scale applies to these). As the lines are in fair agreement with the points and the left-hand and right-hand scales differ only by a constant multiplicative factor, it should be clear that the spectrum of the Crab Nebula must be close to the input spectrum for the simulations.

Table 3 shows how this comparison is converted into a differential spectrum. For each *size* band, the table gives the number of excess events in the on-source field, followed by the weighted number of simulated images in that band. (The numbers observed using $d^2 = 6 - 9$ are extrapolated to $d^2 = 10$ using the smoothed shape of the curves obtained in simulations, as seen in Fig. 9.) The ratio of the observed to simulated numbers, given next, is the factor by which the real flux exceeds the assumed flux in that part of the spectral range. This measured flux is taken to be at the mean energy (weighted by the power-law spectrum), $\langle E \rangle$, of the simulated gamma rays included in this *size*. $\langle E \rangle$ is given in the fifth column. Multiplying the simulated spectrum, $F(E)$, evaluated at the mean energy, $\langle E \rangle$, by the ratio (column 4) and dividing by the total duration of the on-source observations, 74 736 seconds, gives the estimated flux at that energy, and is shown in the last column. These fluxes are plotted in Fig. 13 as solid circles and are close to those derived through Method 1 (open circles). The statistical uncertainties in the simulations are small in comparison to those in the data, and have therefore been ignored.

To a good approximation, $N(\text{excess}) = 0.154 N(\text{sim.})$, so that during the 74 736 seconds of observation there were $0.154 \times 0.1E^{-1.6}$ gamma rays per m⁻² above energy E TeV. Converting this to a differential spectrum gives the result

$$S(E) = (3.30 \pm 0.25) \times 10^{-7} \left(\frac{E}{1 \text{ TeV}} \right)^{-2.60 \pm 0.13} \text{ m}^{-2} \text{ s}^{-1} \text{ TeV}^{-1}, \tag{21}$$

which is very close to the spectrum obtained from Method 1. Because the ratio in the fourth column is virtually constant, the derivation of the true spectrum is simple and unambiguous. For small variations in this ratio, the flux at the mean energies corresponding to the various bands could be derived separately as shown in the last column of the table. If the variation in ratio were not small, one would have to test the correctness of the deduced spectrum by fitting a smooth continuous form, $F_1(E)$, to the deduced flux values, and then predicting again the expected *size* spectrum, using this new $F_1(E)$ to derive the weights. However, with the present database it has been checked that starting with alternative forms of $F(E)$ varying as $E^{-2.4}, E^{-2.6}$ or $E^{-3.0}$ resulted in indistinguishable values for the deduced spectrum, by the method shown in the table, i.e., the initial choice of input spectrum is not critical. The uncertainties are statistical, being derived from the changes in amplitude and exponent needed to increase by 2.3 the value of χ^2 for the fit to the fluxes tabulated in Table 3.

These very wide *size* bands gave only one useful spectral point above 2.1 TeV, so the process was repeated with 1/3 decade *size* bands offset by 1/6 decade from those used initially. This led to estimated differential fluxes of $(1.15 \pm 0.09) \times 10^{-7}$ at 1.52 TeV, $(2.03 \pm 0.24) \times 10^{-8}$ at 3.03 TeV and $(2.5 \pm 0.9) \times 10^{-9}$ at 6.20 TeV, where all flux values are quoted in units of $m^{-2} s^{-1} TeV^{-1}$. It would be probably be desirable in general to use five or six bands per decade rather than three – the wider bands were chosen here to get smoother variations in Fig. 9, as the main emphasis was here on checking the efficiency of the window selection.

4. Discussion

The fluxes derived for the Crab Nebula from both methods are shown in Fig. 13. The 1988/89 data is shown as open circles for Method 1 and as solid circles for Method 2. The 1995/96 data analyzed by Method 1 is indicated by crosses. The solid line shown is a least-squares fit to the combined fluxes for 1988/89 and 1995/96, using Method 1. Also shown is a dashed line indicating the spectrum derived by Vacanti et al. (1991). It is clear that the two methods agree well. We next examine how "robust" the spectra are, i.e., how sensitive they are to small errors in the parameters or simulations. A comparison with other published observations and a discussion of the implications of the spectrum will be taken up in another paper (Hillas et al., 1997).

4.1. Systematic errors: How robust are the methods?

From the discussion in Section 2.4, the Leeds (Hillas, 1995) and ISU simulations agree fairly well with each other and the parameter distributions agree with the gamma-ray data (Section 2.5.2, Fig. 7). However, it is important to gauge the sensitivity of the extracted spectrum to details in the simulations. Systematic errors might arise from the lack of detailed knowledge of various detector parameters. For instance, the overall product of photomultiplier tube gain, electronic gain and mirror reflectivity is not perfectly determined, nor is the atmospheric transmission. This overall gain affects the relationship between the primary energy and the *size*, which is the most important energy estimator. Changes in the overall gain shrink or stretch the energy scale. Because of the form of the spectrum, $S(E) = \alpha E^{-\gamma}$, one expects this to change the flux constant, α and leave the spectral index, γ unchanged. However, γ might also be affected as changes in the gain effectively shifts the location on the area curve, $A(E)$, which can be of importance if this moves the flux points to an energy regime near the threshold where the collection area is still rising.

As described in Section 2.3.3, the relative gain can be scaled from one observation to another. However, determination of the absolute gain and its error is more difficult. Here we will estimate this error by examining each of the composite gain factors. The direct measurement of average pmt gain and its uncertainty (10%) was described earlier in Section 2.3.1. Quantum efficiency as a function of wavelength was measured for two of the pmts, and differences between these responses and the manufacturers average values leads to a 2% standard deviation in the mean of 109 tubes. Measurement of electronic gain/cable losses gives a error of 5%

(Zweerink, 1997). At the start of the 1988/89 observing season the reflector mirrors were freshly recoated, thereby allowing us to estimate an average reflectivity to within about a 10% error, from the background cosmic-ray trigger rate.

Estimation of possible systematic errors arising from atmospheric effects is more complex. In the relevant wavelength regime, essentially all extinction arises from (i) Rayleigh scattering, (ii) ozone absorption, (iii) O_2 absorption and (iv) aerosol scattering. Rayleigh scattering is the dominant mechanism and it is governed by the column density of air above the telescope which is in turn related to barometric pressure. Though atmospheric ozone is located mainly well above shower maximum (roughly 7 km), the tail of the distribution extends to sufficiently low altitudes that it reduces transmission for wavelengths below about 290 nm. Further, O_2 becomes a very effective absorber at about 250 nm. Ozone content varies with season, and there are also uncertainties in the measured O_2 cross sections. Aerosols are located mainly at low altitudes, and the extinction falls with a scale height of roughly 1 km (Jursa, 1985), and are also highly variable.

In order to estimate atmospheric uncertainties, we used the ARTEMIS atmospheric model (Urban et al., 1996) together with a simple aerosol extinction parameterization (Baltrusaitis et al., 1985). The atmospheric transmission from a height of 7 km to the observatory height of 2.3 km was then calculated for several atmospheric models, using an initial Cherenkov spectrum folded with mirror reflectivity and photocathode response and integrating over the wavelength. We found that simultaneously (i) doubling the ozone concentration, (ii) doubling the O_2 absorption cross sections and (iii) doubling the aerosol concentrations from standard values diminished atmospheric transmission by 6%. Conversely, simultaneously halving the same quantities increased transmission by 4%. The background trigger rates are very stable with a typical variation of about 4% at the zenith. This is consistent with highly variable aerosol absorption having a relatively small effect, as found in the model atmospheres. It is also consistent with relatively small changes resulting from pressure variations. We therefore estimate the uncertainty due to atmospheric effects at about 5%.

Combining the uncertainties in all the uncorrelated effects discussed above in quadrature leads to an uncertainty in the overall gain factor of 16%. This is comparable to the uncertainty in the overall gain factor arrived at via comparison of observed cosmic-ray *size* spectra with results from simulations as used in Method 2 (see Section 2.3.2).

There is an additional small systematic error due to the fact that from one to three tubes were switched off in both the on-source and the off-source runs, owing to the presence of a bright star in the field. This might be expected to alter the shapes of the image parameter distributions and consequently affect the entire procedure of spectrum estimation, including the parameter pass bands, collection area and energy estimation function. We have investigated this for the 1988/89 database by turning off tubes in the simulated gamma-ray images in the same pattern as in the data and find that it has minimal effects on the parameter distributions. Only the fits to the *length* and *alpha* distributions are slightly skewed: to an extent which would not be apparent given that the pass bands in these parameters are fairly wide. In the energy regime above the telescope threshold that is of interest here, the collection area and energy estimate are unaffected within the statistical errors in the simulations, so that the final derived spectrum is also the same, within errors.

A final potential problem is the uncertainty in the means of the image parameters. For instance, the mean of the *width* distribution differs slightly in the two simulations (see Fig. 5), and the simulated *alpha* distributions are slightly narrower than is observed in the data (see Section 2.5.2, Fig. 7). Using Method 1, the effect of possible shifts in image parameter distributions has been investigated by widening and narrowing the windows for acceptance of gamma-rays, and noting the effect on the extracted spectrum. Initially, the windows for each selection parameter (*alpha, length, width*) were chosen so that the overall (three-parameter) efficiency for keeping simulated gamma-ray images was 90%. For three test cases, the windows for each parameter were then altered so that the overall efficiencies for keeping simulated gamma-ray images changed to 80%, 85% and 95%, respectively. Within the limits of the statistical errors, there was no difference in the derived spectra. When testing the effect of enlargement of the selection window in Method 2, there is only one window radius to be varied, and the results were shown in Fig. 9. For each of several *size* bands, the points show how the

excess number of selected events, $N_{\text{on}} - N_{\text{off}}$, increases as the size of the ellipsoidal selection window, $d^2_{\max}$, is increased. The lines show the results of applying exactly the same selection to a list of simulated gamma-ray images. One might have expected to adopt a window radius $d^2_{\max} = 6$, to optimize signal-to-noise ratio for four variables. It was found that if a very small window (say, $d^2_{\max} \sim 2$) were chosen, there would be a detectable deficit in numbers due to a slight mis-centering of the window on the predicted mean values of the image parameters. However, for $d^2_{\max}$ in the range 6 to 10 one had a window of the expected efficiency, as increasing the window size in this range only gradually increases the additional number of events accepted. Thus, although there are inevitably small errors in the predicted *width* and *length*, the window-opening test shows that their effect is unimportant.

From the discussion in this section it appears that uncertainty in the overall gain factor is the dominant systematic error. Adopting the 16% value arrived at above leads to a systematic uncertainty of ± 0.6 m^{-2} s^{-1} TeV^{-1} in the flux constant and ± 0.04 in the spectral index.

4.2. Final remarks

The measurement of the energy spectra of TeV gamma-ray sources is a difficult problem that has important implications for the field of gamma-ray astronomy. Besides the usual difficulties faced in detecting TeV gamma-ray sources, one also has to contend with additional problems arising from incomplete knowledge of the telescope calibration and the error in the energy estimate that arises from detector limitations as well as from the fluctuations inherent to the cascade process. As is usual, we have made extensive use of simulations to extract the spectrum of the Crab Nebula.

The two methods described here are largely independent, both in terms of the simulation programs used and in their approach to the problem. Even so, there is very good agreement between the derived spectra and fluxes for the 1988/89 Crab Nebula database, as given in Eqs. (15) and (21), and in Tables 1 and 3. We have tried to estimate the overall telescope gain carefully, cross-checking with several different methods and using a scaling technique to check the calibration between different observing seasons. As the TeV gamma-ray flux from the Crab Nebula is expected to remain steady, we take the good agreement between the derived spectra and fluxes for the two observing seasons (Eqs. (15) and (16), Tables 1 and 2) to be indicative of our success in correctly carrying out the telescope calibration.

We have also investigated several sources of systematic error, including a mis-calibration of the telescope gain and the possibility of errors in the simulation programs. Other areas that have been studied are the errors introduced by operating artifacts such as the turning off of pmts due to the presence of a bright star. The good agreement between results arrived at by different methods gives us faith that we are not being drastically misled by systematic errors. We conclude with the caveat that though the final power-law form of the energy spectra is widely quoted, the derived flux constant, α, and spectral index, γ, have large errors associated with them and attention should also be paid to the fluxes given in Tables 1, 2 and 3, and shown in Fig. 13.

Acknowledgements

Appendix A. Cosmic ray fluxes used in the absolute calibration

The spectra of individual components of cosmic rays are given initially in terms of the variable $U = E/A$, where E is the kinetic energy of the nucleus in GeV and A its atomic mass number, in the form

$$\text{flux} = C \cdot (U + U_0)^{-\gamma} \text{GeV}^{-1} \text{ m}^{-2} \text{ sr}^{-1} \text{ s}^{-1} . \tag{A.1}$$

Fig. A.1 shows the degree of fit of this formula to many data points available in 1993 taking values of C, U_0 and γ from tables in Kaye & Laby (1995), with the exception of U_0 for protons which has been corrected to 4.4 (instead of 2.2). The curves are compared with data points available in 1993, especially from the French–Danish HEAO-3, RICH, Ryan et al. (1972a), and JACEE results. These are essentially the same as the data shown by Swordy (1993). However, the helium fluxes of Ryan et al. (1972a), shown by open symbols, have been excluded from the fit due to their discordant form. It should also be noted that more recent JACEE data on protons in the region of 10–100 TeV lie about 15% lower than the 1993 data, however.

In terms of the total kinetic energy of the nucleus, E, rather than the kinetic energy per nucleon, the spectra can be expressed as

$$\text{flux} = D \cdot (E + E_0)^{-\gamma} \text{GeV}^{-1} \text{ m}^{-2} \text{ sr}^{-1} \text{ s}^{-1} . \tag{A.2}$$

where, $E_0 = A \cdot U_0$ and $D = C \cdot A^{\gamma - 1.0}$. The spectra of the various cosmic-ray components can then be expressed by the parameters in Table A.1 below. For predicting the background spectrum of Cherenkov flash intensities, hadronic showers were simulated for nuclei of mass 1, 4, 16 and 56, with the source points spread uniformly
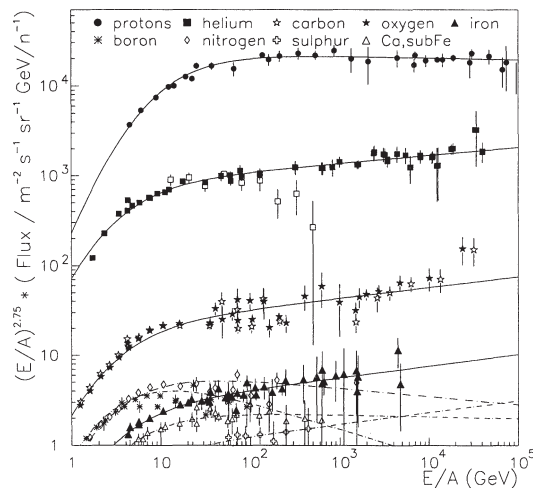

Fig. A.1. The functional forms for the fluxes of cosmic-ray nuclei as used in the Method 2 (ellipsoidal-window) absolute calibration are compared with data available in 1993 (when the fits were made), in order to show the varying degrees of accuracy with which the nuclear fluxes were known. Note that the spectra are plotted here in the conventional manner as functions of kinetic energy per nucleon, rather than total kinetic energy.

Table A.1

Parameters for cosmic-ray fluxes in terms of the total kinetic energy of the incident nucleus

A	1	4	11	12	14	16	20	24	28	32	42	56
D	24500	7390	1637	1091	1028	1744	384	690	774	192	1870	1560
E_0	4.4	5.6	16.5	15.6	21	21	24	29	34	42	71	95
γ	2.77	2.66	3.05	2.63	2.84	2.63	2.62	2.62	2.62	2.62	2.77	2.62

over an area of sky out to $3.5°$ from the center of the telescope field of view. Each spectrum was represented as a power law, the exponents being 2.77, 2.66, 2.63 and 2.62 for the four nuclei, with integral rates above 1 TeV of 0.069, 0.046, 0.035 and 0.022 m^{-2} sr^{-1} s^{-1}, the rates for masses 16 and 56 including the estimated effect of nuclei in the mass range 11–24 and > 27, respectively, assuming for the purpose of combining groups of nuclear types that the Cherenkov output of a nucleus $= A \times f(U)$. (For the mass 56 group, the deviation from a power law caused by the term E_0 should strictly have been included; but our approximation is of little importance as this group only contributes about 4% of the events of *size* greater than 1000 du.)

References

A.S. Jursa, ed., Handbook of Geophysics and Space Environments, 4th ed., available from NTIS (Hanscom Air Force Base, 1985).

C.W. Akerlof, M.F. Cawley, D.J. Fegan, K. Harris, A.M. Hillas, D.J. Jennings, R.C. Lamb, M.A. Lawrence, M.J. Lang, D.A. Lewis, D.I. Meyer, G. Mohanty, K.S. O'Flaherty, M. Punch, P.T. Reynolds, M.S. Schubnell, T.C. Weekes, T. Whitaker, Astrophys. J. Lett. 337 (1991) L97.

Y. Avni, Astrophys. J. 210 (1976) 642.

R.M. Baltrusaitis, R. Cady, G.L. Cassiday, R. Cooper, J.W. Elbert, P.R. Gerhardy, S. Ko, E.C. Loh, M. Salamon, D. Steek, P. Sokolsky, Nucl. Instrum. & Methods Phys. Res. A 240 (1985) 410.

S.D. Biller, C.W. Akerlof, J. Buckley, M.F. Cawley, D.J. Fegan, J.A. Gaidos, A.M. Hillas, A.D. Kerrick, R.C. Lamb, D.A. Lewis, G. Mohanty, H.J. Rose, M.S. Schubnell, G. Sembroski, T.C. Weekes, C. Wilson, in: Proc. 24th Int. Cosmic Ray Conf, Rome, Vol. 3 (1995) pp. 412–415.

M.F. Cawley, D.J. Fegan, K. Harris, A.M. Hillas, P.W. Kwok, R.C. Lamb, M.J. Lang, D.A. Lewis, D. Macomb, P.T. Reynolds, D.J. Schmid, G. Vacanti, T.C. Weekes, Exp. Astron. 1 (1990) 173.

J.W. Cronin, K.G. Gibbs, T.C. Weekes, Ann. Rev. Nucl. Part. Sci. 43 (1993) 883.

D.J. Fegan, Space Sci. Rev. 75 (1996) 137.

A.M. Hillas, in: Proc. 19th Int. Cosmic Ray Conf. La Jolla, Vol. 3 (NASA, Scientific and technical information branch, NASA, Washington D.C., 1985) p. 445.

A.M. Hillas, in: Proc. 24th Int. Cosmic Ray Conf. Rome, Vol. 1 (1995) pp. 270–272.

A.M. Hillas, Space Sci. Rev. 75 (1996) 17, invited talk at Heidelberg Workshop on TeV Astrophysics.

A.M. Hillas et al., Astrophys. J. (1997), in preparation.

G.W. Kaye, T.H. Laby, Tables of Physical and Chemical Constants, 16th ed. (Longman Scientific & Technical, Essex, New York, 1995); originally compiled by G.W. Kaye and T.H. Laby, now prepared under the direction of an editorial committee.

A.D. Kerrick, C.W. Akerlof, S.D. Biller, J.H. Buckey, M.F. Cawley, M. Chantell, V. Connaughton, D.J. Fegan, S. Fennell, J.A. Gaidos, Astro. Phys. J. Lett. 438 (1995) L59.

M.P. Kertzman, G.H. Sembroski, Nucl. Instrum. & Methods Phys. Res. A 343 (1994) 629.

P.W. Kwok, Ph.D. thesis (Univ. of Arizona, Tucson, Arizona, 1989).

M. Lampton, B. Margon, S. Bowyer, R. Cruddace, Astrophys. J. 208 (1976) 177.

D.A. Lewis, C.W. Akerlof, D.J. Fegan, A.M. Hillas, R.C. Lamb, D.I. Meyer, G. Mohanty, T.C. Weekes, in: Proc. 23rd Int. Cosmic Ray Conf., Calgary, Vol. 1, D.A. Leahy, ed. (Dept. of Physics and Astronomy, Univ. of Calgary, Calgary, Canada, 1993) p. 279.

D.J. Macomb, Ph.D. thesis (Iowa State University, Ames, Iowa, 1989).

G. Mohanty, Ph.D. thesis (Iowa State University, Ames, Iowa, 1995).

G. Mohanty, Detector calibration for recent data with the 10m telescope, Whipple Collaboration Internal Report (1997).

G. Mohanty, C.W. Akerlof, M.F. Cawley, D.J. Fegan, S. Fennell, J.A. Gaidos, A.M. Hillas, A.D. Kerrick, R.C. Lamb, D.A. Lewis, D.I. Meyer, M. Punch, A.C. Rovero, M.S. Schubnell, G. Sembroski, T.C. Weekes, C. Wilson, in: Proc. 23rd Int. Cosmic Ray Conf., Calgary, Vol. 1 (Dept. of Physics and Astronomy, Univ. of Calgary, Calgary, Canada, 1993) p. 440.

A.V. Plyasheshnikov, A.C. Konopelko, in: Proc. Int. Workshop on VHE Gamma-Ray Astronomy, Crimea, A.A. Stepanian, D.J. Fegan, M.F. Cawley, eds. (Physics Dept., Univ. College Dublin, 1989) p. 115.

A.V. Plyasheshnikov, A.C. Konopelko, in: Proc. Int. Workshop on VHE Gamma-Ray Astronomy, Crimea, A.A. Stepanian, D.J. Fegan, M.F. Cawley, eds. (Physics Dept., Univ. College Dublin, 1989) p. 120.

M. Punch, C.W. Akerlof, M.F. Cawley, D.J. Fegan, R.C. Lamb, M.A. Lawrence, M.J. Lang, D.A. Lewis, D.I. Meyer, K.S. O'Flaherty, P.T. Reynolds, M.S. Schubnell, in: Proc. 22nd Int. Cosmic Ray Conf. Dublin, Vol. 1 (Dublin Institute for Advanced Studies, 1991) p. 464.

P.T. Reynolds, C.W. Akerlof, M.F. Cawley, M. Chantell, D.J. Fegan, A.M. Hillas, R.C. Lamb, M.A. Lawrence, D.A. Lewis, D. Macomb, D.I. Meyer, G. Mohanty, K.S. O'Flaherty, M. Punch, M.S. Schubnell, G. Vacanti, T.C. Weekes, T. Whitaker, Astrophys. J. 404 (1993) 206.

A.C. Rovero, J.H. Buckley, P. Fleury, Y. Jiang, E. Pare, X. Sarazin, M. Urban, T.C. Weekes, Astropart. Phys. 5 (1996) 27.

M.J. Ryan, J.F. Ormes, V.K. Balasubramanyan, Phys. Rev. Lett. 28 (1972) 985; note that the quoted differential flux is in error, see errata Ryan et al. (1972b).

M.J. Ryan, J.F. Ormes, V.K. Balasubramanyan, Phys. Rev. Lett. 28 (1972) 1497.

D.W. Scott, Biometrika 66 (1979) 605.

S. Swordy, in: Proc. 23rd Int. Cosmic Ray Conf., Calgary, Vol. Invited, Rapporteur & Highlight Papers, D.A. Leahy, R.B. Hicks, D. Venkatesan, eds. (Dept. of Physics and Astronomy, Univ. of Calgary, Calgary, Canada, 1993) p. 243.

M. Urban et al., Nucl. Instrum. & Methods Phys. Res. A 368 (1996) 503.

G. Vacanti, M.F. Cawley, E. Colombo, D.J. Fegan, A.M. Hillas, P.W. Kwok, M.J. Lang, R.C. Lamb, D.A. Lewis, D.J. Macomb, K.S. O'Flaherty, P.T. Reynolds, T.C. Weekes, Astrophys. J. 377 (1991) 467.

T.C. Weekes, Nuovo Cimento B 35 (1976) 95.

T.C. Weekes, M.F. Cawley, D.J. Fegan, K.G. Gibbs, A.M. Hillas, P.W. Kwok, R.C. Lamb, D.A. Lewis, D. Macomb, N.A. Porter, P.T. Reynolds, G. Vacanti, Astrophys. J. 342 (1989) 379.

M. West, Ph.D. thesis (Univ. of Leeds, Leeds, 1994).

J.A. Zweerink, Ph.D. thesis (Iowa State University, Ames, Iowa, 1997).